Available online at www.sciencedirect.com
ScienceDirect
Journal of Computational Physics 219 (2006) 644–670
JOURNAL OF COMPUTATIONAL PHYSICS
www.elsevier.com/locate/jcp

Computing the steady states for an asymptotic model of quantum transport in resonant heterostructures

Virginie Bonnaillie-Noël *, Francis Nier, Yassine Patel

IRMAR, UMR-CNRS 6625, Université Rennes I, Campus de Beaulieu, 35042 Rennes Cedex, France

Received 25 October 2005; received in revised form 6 April 2006; accepted 7 April 2006
Available online 8 June 2006

Abstract

In this article, we propose a rapid method to compute the steady states, including bifurcation diagrams, of resonant tunneling heterostructures in the far from equilibrium regime. Those calculations are made on a simplified model which takes into account the characteristic quantities which arise from an accurate asymptotic analysis of the nonlinear Schrödinger–Poisson system. After a summary of the existing theoretical results, the asymptotic model is explicitly adapted to physically realistic situations and numerical results are shown in various cases.

MSC: 34L25; 34L30; 34L40; 65L10; 65Z05; 82D37

Keywords: Schrödinger–Poisson system; Resonant tunneling diode; Asymptotic model

1. Introduction

Over the past 20 years there has been a serious effort to develop efficient numerical methods in order to compute the steady states of out of equilibrium quantum resonant heterostructures. The final aim is to be able to predict from numerical simulations the I–V characteristic curve for devices which involve an unusual coupling between spectral quantities associated with the quantum mechanics and nonlinear effects due to the electrostatic mean field. Two types of models were considered: purely quantum ones based on Schrödinger–Poisson systems or Wigner–Poisson systems (see for example [1–6,30,34,35]); and quantum hydrodynamic or drift-diffusion models (see for example [9–11,13,36]). The second ones which assume local thermal equilibrium or local entropy maximizing states are well suited for situations where quantum effects, averaged by the statistics over a large number of particles, only bring small corrections to classical mechanics. The first ones on which we will focus stick to the quantum nature of the phenomena and have to be chosen in order to describe accurately the quantum transport. Actually, both of those models were able to recover the negative differential resistance typical of

* Corresponding author. Tel.: +33 2 99 05 93 45; fax: +33 2 99 05 93 28.
E-mail addresses: Virginie.Noel-Bonnaillie@univ-rennes1.fr (V. Bonnaillie-Noël), Francis.Nier@univ-rennes1.fr (F. Nier), Patel@univ-rennes1.fr (Y. Patel).

0021-9991/$ - see front matter
doi:10.1016/j.jcp.2006.04.008

resonant tunneling diodes [9,34,35]. This phenomenon, which is essentially linear, relies on the basic topological argument that, when the bias is increased, the resonant energy eventually crosses the ground energy of the incoming beam. It is therefore very robust, remains in all the considered models and survives to any numerical discretization. The situation became more complicated after the work by Jona-Lasinio et al. [21] and Presilla and Sjöstrand [37], where they showed that the Schrödinger–Poisson system could lead to hysteresis phenomena in agreement with physical observations. Other works mentioned the possibility of having much more complex bifurcation diagrams [22]. In order to catch all these phenomena, an accurate treatment of the tunnel effect through the barrier has to be taken into account and one has to start with quantum models like Schrödinger–Poisson or Wigner–Poisson systems rather than hydrodynamical models. A first difficulty which has to be taken into account is related with the out of equilibrium regime. At the quantum level it can be done in the Landauer–Büttiker [8,25] approach directly on the Schrödinger–Poisson system or via the Wigner–Poisson system [12,14,24]. This has motivated several theoretical studies concerned with the numerical treatment of artificial boundary conditions [1,2], with the well-posedness of the nonlinear problem [5,6,30] and with the derivation of asymptotic models [21,31–33,37]. The second difficulty comes from the complexity of a rough numerical treatment due to the presence of resonant states. The system requires a spatial and a spectral discretization. But resonances lead to very stiff spectral quantities (with slopes like $e^{C/h}$, $h \ll 1$) which require a specific treatment. It was done with WKB techniques in [21] and implemented in numerical methods by Ben Abdallah and Pinaud in [7,34,35]. However, the numerical complexity remains still large enough in order to motivate the derivation of simplified model which would permit a rapid insight of possible bifurcation diagrams.

In [21,37], it is suggested that hysteresis phenomena occur only when the drain barrier is thicker or higher than the source one. Therefore, the geometry of the barriers is an important parameter and it is actually an unknown affected by the nonlinearity even when this latter is not very large. The analysis carried out by the third author on the specific asymptotic model of quantum wells in a semiclassical island was developed in order to elucidate the role of the geometry of the barriers in these nonlinear phenomena. It has been done in a general enough framework in order to cover several heterostructure problems. In doing so, he provided the right quantities which govern the nonlinear phenomenon with an accurate treatment of the tunnel effect. Here we present an adaptation of the theoretical asymptotic analysis which leads to a very rapid determination of bifurcation diagrams.

The outline of the article is the following:

Section 2. *Model*: In this section, we present the nonlinear Schrödinger–Poisson problem with the Landauer–Büttiker approach which involves the stationary scattering states.
Section 3. *Scaling*: We introduce the natural reference magnitudes of this problem. Three numerical dimensionless parameters h, β and γ arise from the scaling of the equations.
Section 4. *Theoretical results*: The results obtained in [32,33] are summarized in the specific regime $h \to 0$.
Section 5. *Validity of the asymptotic model*: On complete numerical computations for the original model, we check that the theoretical asymptotic model in the limit $h \to 0$ is relevant.
Section 6. *Implementation of the asymptotic model*: A distinction is made here between the quantities which come from the asymptotic model and the ones which are computed exactly.
Section 7. *Computation of the Agmon distances*: This short section provides exact analytical expressions for quantities which are involved in the final algorithm.
Section 8. *Penalization method*: Several cases have to be considered. They are separated by multidimensional non-convex constraints. Their implementation is done via a penalization method which is specified in this section.
Section 9. *Numerical results*: Several computations were done for AlGaAs–GaAs or Si–SiO structures and were compared with existing numerical results.
Section 10. *Conclusion*.

2. The model

In resonant tunneling diodes and similar heterostructures, electronic transport occurs transversally to the heterojunctions. It is modelled with a one-dimensional system in the direction $\underline{x} = \underline{x}_3$ which involves mean or

integrated quantities along the two-dimensional parallel direction $(\underline{x}_1, \underline{x}_2)$. The mass m that we use is the effective electronic mass $m = m_3$ in the direction $\underline{x} = \underline{x}_3$ and $\hbar$ denotes the Planck constant.

The quantum Hamiltonian for a single electron has the form

$$-\frac{\hbar^2}{2m}\frac{\mathrm{d}}{\mathrm{d}\underline{x}^2} + \underline{\mathscr{V}}(\underline{x}), \quad \underline{\mathscr{V}} = \underline{\mathscr{B}} + \underline{\mathscr{V}}_0 + \underline{V}_{\mathrm{NL}}, \tag{1}$$

with a nonlinear potential $\underline{V}_{\mathrm{NL}}$ which is non-negative and takes into account the mean repulsive electrostatic field inside the device. It is assumed that these nonlinear effects are negligible (quasineutral approximation) outside the device and we will come back to this point in our conclusion (Section 10). The potential $\underline{\mathscr{V}}$ is the total potential in the device. The first potential term $\underline{\mathscr{B}}$ simply includes the bias voltage $\underline{B}$ applied to the device. It is piecewise affine

$$\underline{\mathscr{B}}(\underline{x}) = -\underline{B}\left[\frac{\underline{x}-a}{b-a}1_{[a,b]}(\underline{x}) + 1_{[b,+\infty)}(\underline{x})\right].$$

The second term describes the barriers and the wells,

$$\underline{\mathscr{V}}_0(\underline{x}) = \underline{V}_0 1_{[a,b]}(\underline{x}) + \sum_{j=1}^{N} \underline{W}_j(\underline{x}),$$

with the constant $\underline{V}_0 > 0$ and the compactly supported potentials $\underline{W}_j \in L^\infty(\mathbb{R})$, $-\underline{V}_0 \leqslant \underline{W}_j \leqslant 0$, fixed. The external potential $\underline{\mathscr{B}} + \underline{\mathscr{V}}_0$ is represented in Fig. 1.

The shape of the incoming beam of electrons is contained in the prescribed function $\underline{f}$. For the initial presentation, we focus on the case of a beam coming from the left-hand side and described by a function $\underline{f}$ supported in $\underline{k} \geqslant 0$. The more physically relevant case where the injection comes from both sides will be discussed further in Section 4.4. We assume that the injection profile is governed by the thermodynamic equilibrium

$$\underline{f}(\underline{k}) = \underline{g}(\underline{k}^2)1_{\mathbb{R}_+}(\underline{k}) \quad \text{with } \underline{g}(\underline{k}^2) = \frac{\sqrt{m_1 m_2}k_{\mathrm{B}}T}{\pi\hbar^2}\ln\left(1+\exp\left(\frac{E_{\mathrm{F}} - \frac{\hbar^2\underline{k}^2}{2m}}{k_{\mathrm{B}}T}\right)\right), \tag{2}$$

where k_{B}, T and $\underline{k}$ denote, respectively, the Boltzmann constant, the temperature and the wave vector, $\underline{g}$ represents the Fermi–Dirac distribution function after integration along the two directions $(\underline{x}_1, \underline{x}_2)$ with $\underline{x} = \underline{x}_3$, and E_{F} is the Fermi level given by

$$E_{\mathrm{F}} = \frac{\hbar^2}{2}(3\pi^2 n_{\mathrm{D}})^{2/3}(m_1 m_2 m_3)^{-1/3}.$$

Here the introduction of a non-isotropic effective electronic mass (m_1, m_2, m_3) permits to apply our model and numerical simulation to heterostructures like Si–SiO. The symbol n_{D} denotes the donor density outside the device $(\underline{x} \notin [a, b])$.

The out-of-equilibrium regime for the Schrödinger–Poisson system requires the introduction of the generalized eigenfunctions in order to describe the steady state density. For a prescribed incoming flow, one uses the incoming generalized eigenfunctions $\underline{\psi}_-(\underline{k}, \underline{x})$ defined for $\underline{k} > 0$ by

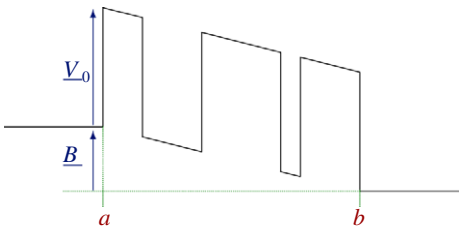

Fig. 1. Representation of the external potential in the device.

$$-\frac{\hbar^2}{2m}\frac{\mathrm{d}^2}{\mathrm{d}\underline{x}^2}\underline{\psi_-}(\underline{k},\underline{x}) + \underline{\mathscr{V}}\underline{\psi_-}(\underline{k},\underline{x}) = \frac{\hbar^2\underline{k}^2}{2m}\underline{\psi_-}(\underline{k},\underline{x}) \quad \text{for } \underline{x}\in\mathbb{R}, \tag{3}$$

$$\underline{\psi_-}(\underline{k},\underline{x}) = \mathrm{e}^{\mathrm{i}\underline{k}\underline{x}} + R(\underline{k})\mathrm{e}^{-\mathrm{i}\,\underline{k}\underline{x}} \quad \text{for } \underline{x}\leqslant a,$$

$$\underline{\psi_-}(\underline{k},\underline{x}) = T(\underline{k})\mathrm{e}^{\mathrm{i}\sqrt{\underline{k}^2+B}\underline{x}} \quad \text{for } \underline{x}\geqslant b,$$

where $R(\underline{k})$ and $T(\underline{k})$ are, respectively, the reflexion and transmission coefficients. The electronic density $\underline{n}$ is then defined by

$$\forall\phi\in\mathscr{C}_c^0((a,b)),\quad \int_a^b \underline{n}(\underline{x})\phi(\underline{x})\,\mathrm{d}\underline{x} = \int_0^{+\infty}\underline{g}(\underline{k}^2)\int_a^b |\underline{\psi_-}(\underline{k},\underline{x})|^2\phi(\underline{x})\,\mathrm{d}\underline{x}\,\frac{\mathrm{d}\underline{k}}{2\pi} = Tr[\underline{f}(K_-)\phi], \tag{4}$$

where K_- is the asymptotic momentum observable (see Section 3.2 and [30]).

Finally, if ϵ denotes the dielectric permittivity and e the elementary charge, the nonlinear potential $\underline{V}_{\mathrm{NL}}$ satisfies the Poisson equation

$$-\frac{\mathrm{d}^2\underline{V}_{\mathrm{NL}}}{\mathrm{d}\underline{x}^2} = \frac{e^2}{\epsilon}\underline{n},\qquad \underline{V}_{\mathrm{NL}}(a) = \underline{V}_{\mathrm{NL}}(b) = 0. \tag{5}$$

3. Scaling the equation

In order to make precisely the connection with the theoretical analysis and for a more flexible numerical treatment (which can be adapted to treat different semiconductor device structures), the Schrödinger–Poisson system is written here with dimensionless quantities and unknowns. The small parameter h is well identified with this writing as the scaled Fermi length.

3.1. Schrödinger equation

The reference length and energy will be the total length of the device $L = b - a$ and the Fermi level E_{F}. With the change of variables $x = \frac{\underline{x}-a}{L}\in[0,1]$, we define the new functions

$$u(x) = \underline{u}(Lx+a) = \underline{u}(\underline{x}) \quad \text{and} \quad \mathscr{V}^h(x) = \frac{1}{E_{\mathrm{F}}}\underline{\mathscr{V}}(Lx+a) = \frac{1}{E_{\mathrm{F}}}\underline{\mathscr{V}}(\underline{x}).$$

The equation

$$-\frac{\hbar^2}{2m}\frac{\mathrm{d}^2}{\mathrm{d}\underline{x}^2}\underline{u} + \underline{\mathscr{V}}\underline{u} = \frac{\hbar^2\underline{k}^2}{2m}\underline{u}$$

becomes

$$-\frac{\hbar^2}{2mL^2E_{\mathrm{F}}}\frac{\mathrm{d}^2}{\mathrm{d}x^2}u + \mathscr{V}^h u = \frac{\hbar^2k^2}{2mE_{\mathrm{F}}}u.$$

The new dimensionless wave vector is given by

$$k = \frac{\hbar}{\sqrt{2mE_{\mathrm{F}}}}\underline{k},$$

while the semiclassical (small) parameter h will be the scaled Fermi length

$$h = \frac{\hbar}{\sqrt{2mE_{\mathrm{F}}}}\frac{1}{L} = \frac{L_{\mathrm{F}}}{L}.$$

Therefore, Eq. (3) is rewritten as

$$-h^2\frac{\mathrm{d}^2}{\mathrm{d}x^2}u+\mathscr{V}^h\,u=k^2u.$$

We write $\mathscr{V}^h$ in the form

$$\mathscr{V}^h(x)=\frac{1}{E_{\mathrm{F}}}\underline{\mathscr{V}}(\underline{x})=\mathscr{B}(x)+\mathscr{V}^h_0(x)+V^h_{\mathrm{NL}}(x),$$

where

$$\mathscr{B}(x)=\frac{1}{E_{\mathrm{F}}}\underline{\mathscr{B}}(\underline{x})=-B[x1_{[0,1]}(x)+1_{[1,+\infty)}(x)],\quad \text{with } B=\frac{\underline{B}}{E_{\mathrm{F}}},$$

$$V^h_{\mathrm{NL}}(x)=\frac{1}{E_{\mathrm{F}}}\underline{V}_{\mathrm{NL}}(\underline{x}),$$

$$\mathscr{V}^h_0(x)=V_0 1_{[0,1]}(x)+\sum_{j=1}^{N}W_j\Big(\frac{x-c_j}{h}\Big)\quad \text{with } W_j\Big(\frac{x-c_j}{h}\Big)=\frac{\underline{W}_j(\underline{x})}{E_{\mathrm{F}}},\quad V_0=\frac{\underline{V}_0}{E_{\mathrm{F}}}.$$

For $h>0$, it is always possible to define $W_j(y)=E_{\mathrm{F}}^{-1}\underline{W}_j(L(c_j+hy))$. The writing $W_j(\frac{x-c_j}{h})$ suggests that the jth well concentrates at $x=c_j$ when $h>0$ is small. The theoretical analysis was carried out in this specific framework by Patel in [32] in the limit $h\to 0$. Actually, this scaling was motivated by the fact that the heterostructures present a finite number of resonant states in the relevant energy interval. The asymptotic of quantum wells $W_j(\frac{x-c_j}{h})$ in a semiclassical island $\mathscr{B}(x)+V^h_{\mathrm{NL}}(x)+V_0 1_{[0,1]}(x)$ permits to keep this constraint even in the limit $h\to 0$. The points c_j can be thought as averaged positions in the wells. They are not exactly the middle points and their determination in practical situations with $h>0$ will be described in Section 6.1.

After calling $\beta=\frac{E_{\mathrm{F}}}{k_{\mathrm{B}}T}=\frac{T_{\mathrm{F}}}{T}$ the ratio between the Fermi temperature and the temperature, the Fermi–Dirac function $\underline{g}$ is transformed into the dimensionless function:

$$g(k^2)=\frac{\pi\hbar^2}{\sqrt{m_1m_2}E_{\mathrm{F}}}\underline{g}(\underline{k}^2)=\beta^{-1}\ln(1+\exp(\beta(1-k^2))).$$

3.2. Generalized eigenfunctions

With the condition $\min W_j\geqslant -V_0$, the Hamiltonian $H^h=-h^2\Delta+\mathscr{V}^h$ has only absolute continuous spectrum (see [32] and references therein). The injection profile in the one-dimensional case is a function of the asymptotic momentum observable K^h_-, according to [6,8,14,25,30]. It is written in terms of the generalized eigenfunctions as

$$f(K^h_-)(x,x')=\int_{-\infty}^{+\infty}f(k)\psi^h_-(k,x)\overline{\psi^h_-(k,x')}\frac{\mathrm{d}k}{2\pi h}. \tag{6}$$

After the scaling, the generalized eigenfunctions for the Hamiltonian H^h satisfy:

$k>0$

$$H^h\psi^h_-(k,x)=k^2\psi^h_-(k,x),$$

$$\psi^h_-(k,x)\sim \mathrm{e}^{\mathrm{i}kx/h}+R(k)\mathrm{e}^{-\mathrm{i}kx/h}\quad \text{for } x\to-\infty, \tag{7}$$

$$\psi^h_-(k,x)\sim T(k)\mathrm{e}^{\mathrm{i}\sqrt{k^2+B}x/h}\quad \text{for } x\to+\infty, \tag{8}$$

$k<0$

$$H^h\psi^h_-(k,x)=(k^2-B)\psi^h_-(k,x),$$

$$\psi^h_-(k,x)\sim \mathrm{e}^{\mathrm{i}kx/h}+R(k)\mathrm{e}^{-\mathrm{i}kx/h}\quad \text{for } x\to+\infty, \tag{9}$$

$$\psi^h_-(k,x)\sim T(k)\mathrm{e}^{-\mathrm{i}(k^2-B)^{1/2}x/h}\quad \text{for } x\to-\infty. \tag{10}$$

The complex square root $(z)^{1/2}$ is chosen above as $(\rho\mathrm{e}^{\mathrm{i}\theta})^{1/2}=\sqrt{\rho}\mathrm{e}^{\mathrm{i}\theta/2}$ for $\rho\geqslant 0$ and $\theta\in[0,2\pi)$.

An important remark in the analysis of [30,32] says that the functions of the energy are specific functions of the momentum. Namely in terms of operator functional calculus, plugging $f(k) = F(k^2)1_{\{k>0\}} + F(k^2 - B)1_{\{k<0\}}$ into (6) leads to $f(K_-^h) = F(H^h)$, when F is any given function of the energy. We refer to [30,32] for more details.

In the case of a beam coming from the left-hand side with a Fermi–Dirac statistics g, the function f is given by $f(k) = g(k^2)1_{\{k>0\}}$ so that

$$f(K_-^h)(x,x') = \int_0^{+\infty} g(k^2)\psi_-^h(k,x)\overline{\psi_-^h(k,x')}\,\frac{\mathrm{d}k}{2\pi h}.$$

The rescaled electronic density is then given as the local trace of $f(K_-^h)$ by

$$n(x) = \int_0^{+\infty} g(k^2)|\psi_-^h(k,x)|^2\,\frac{\mathrm{d}k}{2\pi h} = \frac{\pi\hbar^2}{\sqrt{m_1 m_2}E_\mathrm{F}} L\underline{n}(\underline{x}),$$

after starting from the initial definition

$$\underline{n}(\underline{x}) = \int_0^{+\infty} \underline{g}(\underline{k}^2)\left|\underline{\psi_-}(\underline{k},\underline{x})\right|^2\,\frac{\mathrm{d}\underline{k}}{2\pi}.$$

3.3. Poisson equation

The nonlinear potential $\underline{V}_\mathrm{NL}$ solves

$$-\frac{E_\mathrm{F}}{L^2}\frac{\mathrm{d}^2V_\mathrm{NL}^h(x)}{\mathrm{d}x^2} = -\frac{\mathrm{d}^2\underline{V}_\mathrm{NL}(\underline{x})}{\mathrm{d}\underline{x}^2} = \frac{e^2}{\epsilon}\underline{n}(\underline{x}) = \frac{e^2}{\epsilon}\frac{1}{L}\frac{\sqrt{m_1m_2}E_\mathrm{F}}{\pi\hbar^2}n(x).$$

Therefore, the rescaled nonlinear V_NL^h satisfies the equation

$$-\frac{\mathrm{d}^2V_\mathrm{NL}^h(x)}{\mathrm{d}x^2} = L\frac{e^2\sqrt{m_1m_2}}{\epsilon\pi\hbar^2}n(x).$$

3.4. Scaled system

The previous normalizations are summarized in the rescaled system:

$$\begin{aligned}
&-h^2\frac{\mathrm{d}^2}{\mathrm{d}x^2}\psi_-^h(k,x) + \mathscr{V}^h\psi_-^h(k,x) = k^2\psi_-^h(k,x) + \mathrm{BC},\\
&\mathscr{V}^h(x) = \mathscr{B}(x) + \mathscr{V}_0^h(x) + V_\mathrm{NL}^h(x),\\
&\mathscr{V}_0^h(x) = V_0 1_{[0,1]}(x) - \sum_{j=1}^{N} W_j\Big(\frac{x-c_j}{h}\Big),\\
&g(k^2) = \beta^{-1}\ln(1+\exp(\beta(1-k^2))),\\
&n(x) = \int_0^{+\infty} g(k^2)|\psi_-^h(k,x)|^2\,\frac{\mathrm{d}k}{2\pi h},\\
&-\frac{\mathrm{d}^2V_\mathrm{NL}^h}{\mathrm{d}x^2} = \gamma n, \quad \text{with } V_\mathrm{NL}^h(0) = V_\mathrm{NL}^h(1) = 0,
\end{aligned} \tag{11}$$

where $x = \frac{\underline{x}-a}{L}$, $k = \frac{\hbar}{\sqrt{2mE_\mathrm{F}}}\underline{k}$ and "+BC" summarizes the boundary conditions (7)–(10). The scaling parameters are defined as

$$h = \frac{\hbar}{\sqrt{2mE_\mathrm{F}}}\frac{1}{L} = \frac{L_\mathrm{F}}{L}, \quad \beta = \frac{E_\mathrm{F}}{k_\mathrm{B}T} \quad \text{and} \quad \gamma = \frac{4L}{a_\mathrm{B}}, \tag{12}$$

where the Bohr radius is defined as usual $a_\mathrm{B} = \frac{4\pi\hbar^2\epsilon}{\sqrt{m_1m_2}e^2}$. Thus h is the scaled Fermi length, β the scaled Fermi energy and γ^{-1} the scaled Bohr radius.

3.5. Current

Although the current density $\underline{J}$ is a final quantity which will always be presented in its physical units, the rescaled density current J satisfies

$$J = \int_0^{+\infty} g(k^2)\mathrm{Im}\left(\int_0^1 \frac{\mathrm{d}\psi_-^h(k,x)}{\mathrm{d}x}\overline{\psi_-^h(k,x)}\,\mathrm{d}x\right)\frac{\mathrm{d}k}{2\pi h}, \tag{13}$$

while the scaling is $\underline{J} = \frac{e\sqrt{m_1 m_2}}{m}\frac{E_F}{\pi\hbar L^2}J$.

4. Theoretical results

This section gives a short account of the theoretical results which were obtained in [32] about the limit $h \to 0$ for the scaled system (11). After this presentation, it will be shown how the simple asymptotic model can be extended in order to include physically relevant situations.

4.1. Linear case

Consider first a quantum Hamiltonian $H^h = -h^2\mathrm{d}^2/\mathrm{d}x^2 + \mathscr{V}^h$ where the potential $\mathscr{V}^h$ is defined according to (11) with the nonlinear potential V_{NL}^h replaced by a non-negative potential $V^h(x)$. Another change in the theoretical analysis is about the beam profile g which is replaced by a compactly supported function $\tilde{g}$.

Assumption 1. The family $(V^h)_{h\in(0,1)}$ is assumed to be uniformly bounded in the space of Lipschitz functions $W^{1,\infty}([0,1])$ with a limit V in the $\mathscr{C}^0([0,1])$ topology.

Assumption 2. The function $\tilde{g}$ (which replaces the function g in (11)) is a continuous function with a compact support included in $[\Lambda_*, \Lambda^*] \subset (0, V_0 - B)$. Moreover, the potentials W_j are compactly supported and satisfy $-V_0 \leqslant W_j \leqslant 0$.

Notations

- The potential $\tilde{\mathscr{V}}$ is the limiting filled (i.e. where the wells W_j have been removed) potential[1]

$$\tilde{\mathscr{V}}(x) = \mathscr{B}(x) + V_0 1_{[0,1]}(x) + V(x).$$

- For any $j = 1,\ldots,N$, the Schrödinger operator $H_j := -\mathrm{d}^2/\mathrm{d}x^2 + W_j(x)$, $D(H_j) = H^2(\mathbb{R}) \subset L^2(\mathbb{R})$, admits a finite number of negative eigenvalues $(-e_j^k)_{1\leqslant k\leqslant K_j<+\infty}$ labelled according to the increasing order. The set of energies $\mathscr{E}_j$ is defined by

$$\mathscr{E}_j = \left\{\tilde{\mathscr{V}}(c_j) - e_j^k,\ 1 \leqslant k \leqslant K_j\right\}. \tag{14}$$

- The quantities e_j^k, $1 \leqslant k \leqslant K_j$, $1 \leqslant j \leqslant N$ are called the resonant depths.
- The set of resonant energies is defined as

$$\mathscr{E} = \bigcup_{j=1}^{N}\mathscr{E}_j = \left\{\tilde{\mathscr{V}}(c_j) - e_j^k,\ 1 \leqslant k \leqslant K_j,\ 1 \leqslant j \leqslant N\right\}. \tag{15}$$

- For any $E \in \mathbb{R}$, we set

$$J^E := \{j \in \{1,\ldots,N\} \quad \text{s.t. } E \in \mathscr{E}_j\}.$$

We say that the well c_j is resonant at the energy E when $j \in J^E$.

- Finally, we set

[1] Similarly, for $h > 0$, we use the notation $\tilde{\mathscr{V}}^h(x) = \mathscr{B}(x) + V_0 1_{[0,1]}(x) + V^h(x)$.

$$c_\ell^E := \min_{j\in J^E} c_j, \quad c_r^E := \max_{j\in J^E} c_j,$$

and simply

$$c^E \quad \text{when } c_\ell^E = c_r^E.$$

Definition 3. For $\Phi \in L^\infty([0,1];\mathbb{R})$, the Agmon distance is the degenerate distance given by

$$d_{\mathrm{Ag}}(x,y;\Phi) = \left|\int_x^y \sqrt{\Phi_+(t)}\,\mathrm{d}t\right|,$$

with $\Phi_+(t) = \max\{\Phi(t),0\}$.

For a resonant energy $E \in \mathscr{E}$, we set

$$\delta_\ell^E := d_{\mathrm{Ag}}(c_r^E,1;\tilde{\mathscr{V}}-E) - d_{\mathrm{Ag}}(0,c_r^E;\tilde{\mathscr{V}}-E),$$
$$\delta_r^E := d_{\mathrm{Ag}}(0,c_\ell^E;\tilde{\mathscr{V}}-E) - d_{\mathrm{Ag}}(c_\ell^E,1;\tilde{\mathscr{V}}-E).$$

Remark 4. The Agmon distance is a standard tool in the analysis of WKB methods (see for example [18]) and solves locally an Hamilton–Jacobi equation. It is usually referred to in the physics literature as the action.

With this definition, $\delta_\ell^E > 0$ if and only if all the resonant wells at the energy E are in the left-hand side of the island (i.e. closer to $x=0$ than $x=1$). Conversely, $\delta_r^E > 0$ if and only if all the resonant wells at the energy E are in the right-hand side of the island (i.e. closer to $x=1$ than $x=0$). Actually, for $x,y \in [0,1]$, the distance with the asymptotic potential has to be thought as the limit

$$d_{\mathrm{Ag}}(x,y;\tilde{\mathscr{V}}-E) = \lim_{h\to 0} d_{\mathrm{Ag}}(x,y;\tilde{\mathscr{V}}^h-E) = \lim_{h\to 0} d_{\mathrm{Ag}}(x,y;\mathscr{V}^h-E).$$

Instead of writing explicitly a theorem which would require additional technical (and sometimes artificial) mathematical assumptions, we simplify here the presentation of the results obtained in [31,32]. We refer the reader to those references for more precise statements.

Result 1: The electronic density defined by

$$n^h(x) = \int_0^{+\infty} \tilde{g}(k^2)\left|\psi_-^h(k,x)\right|^2 \frac{\mathrm{d}k}{2\pi h}$$

defines a non-negative measure in $[0,1]$ which admits weak* limit points in the set $\mathscr{M}_b([0,1])$ of bounded Radon measures on $[0,1]$ as $h \to 0$. With Assumptions 1 and 2, those limit points take the form in $]0,1[$

$$\mu|_{]0,1[}(x) = \sum_{E\in\mathscr{E}} \sum_{j\in J^E} t_j^E \tilde{g}(E)\delta_{c_j}(x),$$

where δ_{c_j} denotes the Dirac δ-function and the coefficients t_j^E satisfy[2]

$$t_j^E \in [0,1] \quad \text{and} \quad \begin{cases} \delta_\ell^E > 0 \Rightarrow t_j^E = 1 & \forall j \in J^E, \\ \delta_r^E > 0 \Rightarrow t_j^E = 0 & \forall j \in J^E. \end{cases} \tag{16}$$

Generic case: The non degenerate case is when $\#J^E = 1$ with $\delta_\ell^E > 0$ or $\delta_r^E > 0$ for all $E \in \mathscr{E} \cap \mathrm{supp}\tilde{g}$. Then the sequence $n^h|_{]0,1[}$ admits a unique limit point:

$$n^h|_{]0,1[}(x) \overset{h\to 0}{\rightharpoonup} \sum_{E\in\mathscr{E}} 1_{\delta_\ell^E>0}(E)\tilde{g}(E)\delta_{c^E}(x).$$

Critical case 1: Already with one resonant state, $\mathscr{E} \cap \mathrm{supp}\tilde{g} = \{E_0\}$ with $\#J^{E_0} = 1$, a non generic case may appear. It corresponds to the case $\delta_\ell^{E_0} = \delta_r^{E_0} = 0$:

[2] The corresponding results in [31] are written with a sign mistake.

$$d_{\mathrm{Ag}}(0, c^{E_0}; \tilde{\mathscr{V}} - E_0) = d_{\mathrm{Ag}}(c^{E_0}, 1; \tilde{\mathscr{V}} - E_0). \tag{17}$$

It was shown that this asymptotic information on the Agmon distances (it is written in terms of the asymptotic potential $\tilde{\mathscr{V}}$) does not prevent any value $t_1^{E_0} \in [0,1]$. Note that the indeterminacy of $t_1^{E_0}$ is replaced by the constraint (17).

Critical case 2: Another interesting case which is considered by our numerical calculations is about the case $\#J^{E_0} = 2$ (for the sake of simplicity we assume here again $\mathscr{E} \cap \mathrm{supp}\tilde{g} = \{E_0\}$). First, since E_0 is a limiting resonant energy (i.e. the limit as $h \to 0$ of the real part of a resonance), all the cases when E_0 is the common limit of two distinct h-dependent resonant energies have to be considered. In particular, the generic case and any relevant combination of the critical case 1 can still occur. Once this is done, another case is possible when $\delta_\ell^E \leqslant 0$ and $\delta_r^E \leqslant 0$. The possible values of $t_1^{E_0}$ and $t_2^{E_0}$ can be restricted to the next three cases:

$$t_1^{E_0} = 1, \quad t_2^{E_0} \in [0,1], \quad \text{when } d_{\mathrm{Ag}}(0, c_\ell^{E_0}; \tilde{\mathscr{V}} - E_0) < d_{\mathrm{Ag}}(c_r^{E_0}, 1; \tilde{\mathscr{V}} - E_0), \tag{18}$$

$$t_1^{E_0} \in [0,1], \quad t_2^{E_0} = 0, \quad \text{when } d_{\mathrm{Ag}}(0, c_\ell^{E_0}; \tilde{\mathscr{V}} - E_0) > d_{\mathrm{Ag}}(c_r^{E_0}, 1; \tilde{\mathscr{V}} - E_0), \tag{19}$$

$$0 \leqslant t_2^{E_0} \leqslant t_1^{E_0} \leqslant 1, \quad \text{when } d_{\mathrm{Ag}}(0, c_\ell^{E_0}; \tilde{\mathscr{V}} - E_0) = d_{\mathrm{Ag}}(c_r^{E_0}, 1; \tilde{\mathscr{V}} - E_0). \tag{20}$$

Such a result can be obtained by considering all the possible asymptotic behaviour of the explicit h-dependent quantities computed in [32, pp. 250–256]. Cases where more than two resonant energies can meet (i.e. when $\#J^E > 2$) will not be considered and the above enumeration will be taken for granted in our asymptotic model.

4.2. Nonlinear asymptotics

Here are the mathematical results which were rigorously proved in [32,33] with Assumptions 1 and 2.

We introduce the functional spaces $BV^2([0,1])$ of continuous functions whose second derivative is a bounded measure on $[0,1]$ and its subspace

$$BV_0^2([0,1])_+ = \{V \in BV^2([0,1]) \text{ s.t. } V \geqslant 0, V(0) = V(1) = 0\}.$$

Note the embedding $BV_0^2([0,1])_+ \subset BV^2([0,1]) \subset \mathscr{C}^{0,\alpha}([0,1])$ where the last one is compact for any $\alpha \in (0,1)$.

By setting $c_0 = 0$ and $c_{N+1} = 1$, we introduce the set of piecewise affine functions:

$$\mathbb{P}_0^1(\mathbf{c})_+ := \left\{V \in \mathbb{P}^1(\mathbf{c}),\ V \geqslant 0\right\},$$

with $\mathbb{P}^1(\mathbf{c})$ the usual set of continuous $\mathbb{P}^1$ finite elements associated with the nodes $\mathbf{c} = \{c_0, c_1, \ldots, c_{N+1}\}$, $c_0 = 0$, $c_{N+1} = 1$.

Theorem 5. *Under Assumptions 1 and 2 (with g replaced by $\tilde{g}$ in (11)), the solutions V_{NL}^h, $h \in (0,1]$, of the system (11)*

$$-\frac{\mathrm{d}^2 V_{\mathrm{NL}}^h}{\mathrm{d}x^2} = \gamma n,$$
$$V_{\mathrm{NL}}^h(0) = V_{\mathrm{NL}}^h(1) = 0$$

describe a bounded set of $BV_0^2([0,1])_+$. The set $\mathscr{A}$ of its limit points as $h \to 0$ is a subset of $\mathbb{P}_0^1(\mathbf{c})_+$. Moreover, any $V \in \mathscr{A}$ solves

$$-\frac{\mathrm{d}^2 V}{\mathrm{d}x^2} = \gamma \sum_{E \in \mathscr{E} \cap [A_*, A^*]} \sum_{j \in J^E} t_j^E \tilde{g}(E) \delta_{c_j}, \quad V(0) = V(1) = 0, \tag{21}$$

where the coefficients t_j^E satisfy

$$t_j^E \in [0,1] \quad \textit{and} \quad \begin{cases} \delta_\ell^E > 0 \Rightarrow t_j^E = 1 \quad \forall j \in J^E, \\ \delta_r^E > 0 \Rightarrow t_j^E = 0 \quad \forall j \in J^E. \end{cases} \tag{22}$$

Let $\mathscr{C}$ be the set

$$\mathscr{C} := \{V \in \mathbb{P}^1_0(\mathbf{c})_+ \text{ s.t. } \forall E \in \mathscr{E} \cap [\Lambda_*, \Lambda^*],\ (\delta^E_\ell > 0 \text{ or } \delta^E_r > 0)\}.$$

The possible limits lying in $\mathscr{C}$ can be given by a variational formulation using

$$G(E) = -\int_E^{+\infty} \tilde{g}(\lambda)\, \mathrm{d}\lambda.$$

Corollary 6. *The set $\mathscr{A} \cap \mathscr{C}$ is given by the collection of critical points in $\mathbb{P}^1_0(\mathbf{c})_+$ for the functionals*

$$\mathscr{J}_{\mathscr{K}}(V) = \frac{1}{2}\int_0^1 \left|\frac{\mathrm{d}V(x)}{\mathrm{d}x}\right|^2 \mathrm{d}x - \sum_{E\in\mathscr{K}} G(E), \tag{23}$$

which satisfy the compatibility condition

$$\mathscr{K} = \left\{E \in \mathscr{E} \cap [\Lambda_*, \Lambda^*] \text{ s.t. } \delta^E_\ell > 0\right\}.$$

The previous result covers in a slightly wider generality what we called the "generic case" in the previous subsection. It does not say anything about $\mathscr{A} \setminus \mathscr{C}$. Actually, Theorem 5 can be combined with the discussion of Section 4.1 in order to get a full description, possibly too wide, of $\mathscr{A}$. The important conclusion stemming from Theorem 5 is that it reduces an infinite dimensional nonlinear system which couples in a non-trivial way spectral quantities with an elliptic PDE, to a collection of simple finite dimensional nonlinear systems. Moreover, a full description of this collection of nonlinear systems involves the comparison of some Agmon distances.

Before going further in this direction, we first present how the theoretical results have to be interpreted and adapted in order to fit with the more realistic model.

4.3. Realistic injection profile

Assumption 2 about the compact support of $\tilde{g}$ is a technical assumption which simplifies at different points the mathematical analysis. Of course it is not satisfied by the Fermi–Dirac distribution function g in (11). The two extremal values $+\infty$ and 0 are analyzed on different bases.

First the Fermi–Dirac distribution function decays exponentially fast with respect to the energy like any thermodynamical equilibrium distribution function. Truncating at high energy is physically relevant and necessary for a numerical treatment. The assumption that the compact support of g is included in $[0, \Lambda^*] \subset [0, V_0 - B)$ can be extended to $[0, \Lambda^*] \subset [0, V_0)$. It will be relevant for realistic physical data provided that the temperature T and the donor density n_{D} are not too high (with our dimensionless parameter $V_0 > 1$ and β large enough).

The treatment of the energy 0 has to be done with more care. Actually, it is known that the crossing of the energy 0 by the resonant energies explains the negative differential resistance or the hysteresis phenomenon. A complete rigorous mathematical approach can be performed by starting from Theorem 5 as follows:

(0) Replace the function g in (11) by a function compactly supported in $[0, \Lambda^*] \subset [0, V_0)$.
(1) Take a function $\chi \in \mathscr{C}^\infty(0, +\infty)$ such that $\chi \equiv 1$ on $[1, +\infty)$ and $\chi \equiv 0$ for $[0, 1/2]$.
(2) Set for $\varepsilon > 0$, $\tilde{g}_\varepsilon(x) = \chi(\frac{x}{\varepsilon})g(x)$.
(3) Denote by $\mathscr{V}^{\varepsilon,h}_{\mathrm{NL}}$ the possible solutions of the system (11) with g replaced by $\tilde{g}_\varepsilon$.
(4) Consider the two steps asymptotics as $\varepsilon \to 0$ after $h \to 0$.

According to Theorem 5 and for any $\varepsilon > 0$, the limit points of $V^{\varepsilon,h}_{\mathrm{NL}}$ describe a bounded set $\mathscr{A}^\varepsilon$ of piecewise affine potentials which solve (21) with $\tilde{g}$ replaced by $\tilde{g}_\varepsilon$. The possible limits as $\varepsilon \to 0$ belong to the set $\mathscr{A}$ of solutions to

$$-\frac{\mathrm{d}^2 V}{\mathrm{d}x^2} = \gamma \sum_{E\in\mathscr{E}\cap[0,\Lambda^*]} \sum_{j\in J^E} t^E_j g(E)\delta_{c_j}, \quad V(0) = V(1) = 0, \tag{24}$$

where $g(0) \in [0, g(0^+)]$ is arbitrary, and where the coefficients t_j^E satisfy

$$t_j^E \in [0,1] \quad \text{and} \quad \begin{cases} \delta_\ell^E > 0 \Rightarrow t_j^E = 1 & \forall j \in J^E, \\ \delta_r^E > 0 \Rightarrow t_j^E = 0 & \forall j \in J^E. \end{cases} \tag{25}$$

In connection with the variational formulation of Corollary 6, an interesting property related in some sense to the thermodynamical stability is due to the fact that g is a decaying function. Set

$$\dot{\mathscr{C}} := \left\{ V \in \mathbb{P}_0^1(\mathbf{c})_+ \text{ s.t. } 0 \notin \mathscr{E} \text{ and } \forall E \in \mathscr{E} \cap (0, \Lambda^*],\ (\delta_\ell^E > 0 \text{ or } \delta_r^E > 0) \right\},$$

and

$$G(E) = -\int_E^{\Lambda^*} g(\lambda)\, \mathrm{d}\lambda, \quad \text{for } E \in [0, \Lambda^*].$$

Proposition 7. *The set $\mathscr{A} \cap \dot{\mathscr{C}}$ is given by the collection of critical points in $\mathbb{P}_0^1(\mathbf{c})_+$ for the functionals of the form (23) which satisfy the compatibility condition*

$$\mathscr{K} = \left\{ E \in \mathscr{E} \cap (0, \Lambda^*] \text{ s.t. } \delta_\ell^E > 0 \right\}, \quad 0 \notin \mathscr{E}.$$

When g is decreasing on $(0, \Lambda^*)$, the functional $\mathscr{J}_{\mathscr{K}}$ is strictly convex for any fixed $\mathscr{K}$ and there exists at most one critical point.

Hence for generic cases which avoid $0 \in \mathscr{E}$, the problem is reduced to a finite collection of well-posed variational nonlinear problems in finite dimension.

4.4. Injection from the two sides

For the sake of simplicity but also for a pedagogical purpose, the mathematical analysis as well as the above presentation were done in the case where the function of the momentum $g(k)$ is supported in $\{k \geqslant 0\}$. This presentation makes more clear the spectral anisotropy when functions of the momentum are considered instead of functions of the energy. However in realistic diodes, electrons are injected from both sides with different electro-chemical potentials (see Fig. 2). Actually, this two-sided injection of electrons is easily taken into account in the modelling or in the mathematical analysis as follows.

Let us denote by g_+ and g_- the (truncated) Fermi–Dirac function for the injection profiles from the left and from the right, respectively. When the donor density are equal in the source and in the drain, taking into account the height of the bias B provides

$$g_+(E) = g_0(E) \quad \text{and} \quad g_-(E) = g_0(E + B).$$

Since the momentum function has the form

$$g(k) = g_+(k^2) 1_{\{k>0\}} + g_-(k^2 - B) 1_{\{k<0\}},$$

we can write

$$g(k) = (g_+(k^2) - g_-(k^2)) 1_{\{k>0\}} + (g_-(k^2 - B) 1_{\{k<0\}} + g_-(k^2) 1_{\{k>0\}}).$$

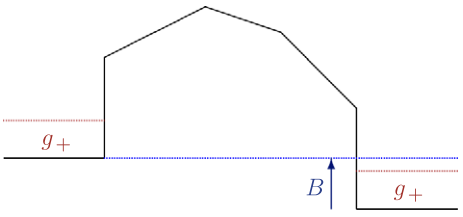

Fig. 2. Injection from the two sides.

Using the decomposition of the incoming beam in a part coming from the left-hand side and one other coming from the right-hand side, the operator form of this identity becomes

$$g_+(H^h)1_{\{K^h>0\}} + g_-(H^h)1_{\{K^h<0\}} = (g_+(H^h) - g_-(H^h))1_{\{K^h>0\}} + g_-(H^h). \tag{26}$$

The first part of the right-hand side of (26) is a function of the momentum supported in $k > 0$ and the second is a function of the energy.

Hence Theorem 5 and its variation of Section 4.3 can be adapted by replacing $g(E)$ by $g_+(E) - g_-(E)$ in (24) while adding a term $g_-(E)$ without any coefficient t_j^E.

The set $\mathscr{A}$ of possible limit points of solutions to (11) with a two-sided injection is the set of non-negative piecewise affine potentials which solve

$$\begin{aligned} -\frac{\mathrm{d}^2V}{\mathrm{d}x^2} &= \gamma \sum_{E\in\mathscr{E}} \sum_{j\in J^E} \left(t_j^E (g_+(E) - g_-(E)) 1_{\{[0,\Lambda^*]\}}(E) + g_-(E) 1_{[0,\Lambda^*]}(E) \right) \delta_{c_j}, \\ V(0) &= V(1) = 0, \end{aligned} \tag{27}$$

with the convention that $(g_+ - g_-)(0)$ can be any value in $[0, (g_+ - g_-)(0^+)]$ and where the coefficients t_j^E satisfy the property (25).

Moreover, the variational formulation of Proposition 7 can be adapted with a similar uniqueness result when g_0 is a decreasing function.

4.5. Conclusion about the theoretical analysis

The theoretical results show that, asymptotically as $h \to 0$, the full system (11) reduces to a collection of well-posed simple nonlinear equations. The well-posedness is confirmed by the uniqueness result of Proposition 7 for some generic case. Another important point which appeared in the discussion of Section 4.1 is that, in all the degenerate cases which were considered, any new indeterminacy of the coefficients t_j^E is compensated by a new equation. Similarly, the indeterminacy of $g(0)$ in (24) (resp. of $(g_+ - g_-)(0)$ in (27)) is compensated by the equation $E = 0$.

Moreover, this mathematical analysis shows what are the important quantities in this nonlinear problem. Asymptotically and for any fixed case (generic or critical case), the unknowns are reduced to the jumps of the potential derivative $\mathrm{d}V/\mathrm{d}x$:

The set of unknowns is the finite set of total masses per well.

The important parameters are:

- The dimensionless small parameter $h \to 0$: In practical situations, the parameter h is strictly positive but reasonably small in order to exhibit resonances as very stiff spectral quantities. Remind that the asymptotic analysis was carried out in a framework which keeps a finite number of resonant states in the physically relevant energy interval. This fits very well with the cases which will be presented.
- The position of the well c_j: In the mathematical analysis, the quantum wells are asymptotically pointwise concentrated. Of course, this does not hold exactly for realistic $h > 0$. These positions will be computed as averaged positions in the wells around which the electronic density concentrates.
- The bound state energies $-e_j^k$ of the Hamiltonian $-\Delta + W_j$: After a translation by $\tilde{V}(c_j)$, they are equal to the real part of the resonances or to the Dirichlet eigenvalues up to some very small error (this will be checked numerically). Those energies are parameters of the asymptotic nonlinear problem. They will be computed numerically in a linear setting before being plugged into the computation of the nonlinear solutions. Actually, as we will see in Section 6.1, the parameters $-e_j^k$ and c_j will be determined similarly by the same process.
- The Agmon distances: Although they are unknowns before solving the nonlinear problem, they can be viewed as parameters in the sense that the comparison of Agmon distances parametrizes all the possible cases. Actually, all the possible cases are considered in a first numerical approach and the constraints on

the Agmon distances are checked afterwards in order to eliminate the irrelevant cases. Note also that the fact that for $h > 0$, the wells are not pointwise concentrated has to be taken into account in the computation of the actual Agmon distances. The details are explained in Section 7.

5. Validity of the asymptotic model

Here it is checked on some numerical examples that the asymptotics $h \to 0$ makes sense in the simulation of realistic devices. Some examples of electronic densities, numerically computed with a large number of generalized eigenfunctions, exhibit an anisotropy phenomenon which confirms the rapid variation of the asymptotic parameter t_j^E from 1 to 0 in (24). All those numerical observations are presented in order to show that the asymptotic model derived as the dimensionless parameter h goes to 0 makes sense in the study of realistic devices.

5.1. Generalized eigenfunctions

In one dimension and with the potential $\mathscr{V}^h$ which is constant outside $[0,1]$, the generalized eigenfunctions are fully determined by a k-dependent non-homogeneous boundary problem on $[0,1]$.

Let us first consider the case $k > 0$. The incoming generalized eigenfunction is then characterized by $\psi_-^h(k)$:

$$\begin{aligned} &-h^2 \frac{\mathrm{d}^2}{\mathrm{d}x^2}\psi_-^h(k,x) + \mathscr{V}^h\psi_-^h(k,x) = k^2\psi_-^h(k,x), \\ &h\psi_-^{h\,\prime}(k,0) + \mathrm{i}k\psi_-^h(k,0) = 2\mathrm{i}k, \qquad\qquad k > 0, \\ &h\psi_-^{h\,\prime}(k,1) - \mathrm{i}\sqrt{k^2+B}\,\psi_-^h(k,1) = 0. \end{aligned} \tag{28}$$

In the case $k < 0$, $k^2 \neq B$, with the convention $(k^2-B)^{1/2} = \mathrm{i}\sqrt{B-k^2}$ when $B > k^2$ (more generally $(\rho \mathrm{e}^{\mathrm{i}\theta})^{1/2} = \sqrt{\rho}\mathrm{e}^{\mathrm{i}\theta/2}$ for $\rho > 0$ and $\theta \in [0,2\pi)$), the generalized eigenfunction $\psi_-^h(k)$ is given by

$$\begin{aligned} &-h^2 \frac{\mathrm{d}^2}{\mathrm{d}x^2}\psi_-^h(k,x) + \mathscr{V}^h\psi_-^h(k,x) = (k^2-B)\psi_-^h(k,x), \\ &h\psi_-^{h\,\prime}(k,0) + \mathrm{i}(k^2-B)^{1/2}\psi_-^h(k,0) = 0, \qquad\qquad k < 0, \\ &h\psi_-^{h\,\prime}(k,1) + \mathrm{i}k\psi_-^h(k,1) = 2\mathrm{i}k\mathrm{e}^{\mathrm{i}k/h}. \end{aligned} \tag{29}$$

Numerically, those boundary value problems are simply computed by a finite difference method. The discretization step $\Delta_x = 1/N_x$ is a parameter of the numerical method. The computation of integrated quantities with respect to k also requires a discretization in the k variable. The step Δ_k has to be chosen small enough in order to catch the resonances which produce very stiff spectral quantities when $h > 0$ is small. Actually, it is known (see for example [19,20,38]) that this slope is of order $\mathrm{e}^{C/h}$. The stiffness of this spectral quantities is a first test to check that the asymptotic model for $h \to 0$ is relevant. One may question about the numerical complexity related to the choice of a very small $\Delta_k = \Lambda^*/N_k$. Actually, such calculations are done only once in the beginning in order to guess the parameters $-e_j^k$ (and c_j, see Section 6.1) and in the end in the computation of the current density (see Section 6.2). Once those parameters are fixed, solving the asymptotic nonlinear problem (24) does not involve anymore the generalized eigenfunctions. Hence the numerical complexity of the accurate computations of the generalized eigenfunction is not a big issue here. For the alternative efficient numerical methods related to such problems and which deal with the generalized eigenfunctions on the ground of a WKB analysis, we refer to the works of Ben Abdallah and Pinaud [7,34,35].

5.2. Detection of resonances

After computing the generalized eigenfunctions by a finite difference method, we compute the local density of states with respect to the energy in each well. The stiff peaks of this density of states are identified as

resonances according to the Breit–Wigner formula (see [15,32,38]). Note that for $h > 0$, the wells are not reduced to single points. We define for each well around c_j, the function

$$M_j(E) = \int_{[c_j^-, c_j^+]} \left(|\psi_-^h(\sqrt{E}, x)|^2 + |\psi_-^h(-\sqrt{E+B}, x)|^2 \right) \mathrm{d}x.$$

The neighbourhood $[c_j^-, c_j^+]$ of the center of the well c_j is specified further in Section 7.

Fig. 3 shows the function $M_1(E)$ in a fixed well for two values $B = 0 = B_{\min}$ and $B = B_{\max}$ of the bias. It corresponds to the physically realistic case with one well presented in Section 9.2, case 1. We simply show the results in terms of dimensionless quantities. The errorbar on the energy axis represents the detected resonances and the Dirichlet eigenvalues (with boundary conditions $\psi(0) = \psi(1) = 0$ instead of transparent boundary conditions in (29)). The very stiff picks as well as the proximity of the detected resonances with the Dirichlet eigenvalues confirm the validity of an asymptotic treatment as $h \to 0$.

5.3. Filled and empty wells for functions of the momentum

On the ground of numerical examples, we now show that the asymptotic behaviour described in (22) makes sense even when $h > 0$ is not very small and lies in the range of parameters occurring in realistic configurations. We simply consider here two asymmetric barrier profiles which are related to the examples of Section 9.2.

The bias is 0 as well as the nonlinear potential. Instead of changing the potential, we consider the two injection profiles

$$\text{injection from the left :} \quad g(k) = (1 - k^2)_+ 1_{[0,+\infty)}(k),$$
$$\text{injection from the right :} \quad g(k) = (1 - k^2)_+ 1_{(-\infty,0]}(k).$$

Let us first analyze the device described in Fig. 4. For this device with one well, we have $h = 0.17$. The size of the barriers are, respectively, 0.5 and 0.8 nm and the width of the well is 4 nm. With electrons coming from the left-hand side, then the well c is filled. This illustrates the case $t_1 = 1$ in (22). With electrons coming from the right-hand side, then the well c is not filled. This illustrates the case $t_1 = 0$ in (22). Note that $h = 0.17$ is not very small and that the width of the barriers does not show a big asymmetry. This example is investigated in Section 9.2, case 1. Here, the size of the barriers and the wells have been changed a little in order to emphasize the Agmon distance effects.

Actually, in examples associated with GaAs devices, the transition from $t_1 = 1$ to $t_1 = 0$ is even more sensitive to the variation of the widths of the barriers.

Fig. 5 shows a device with two wells. The widths of barriers are, respectively, 0.5, 0.5 and 0.6 nm and the widths of the wells are 1.5 and 1 nm. In this device, we have $h = 0.13$ and there is one resonant state per well, with resonant energies $\mathscr{E} = \{E_1, E_2\}$. The corresponding Agmon distances satisfy

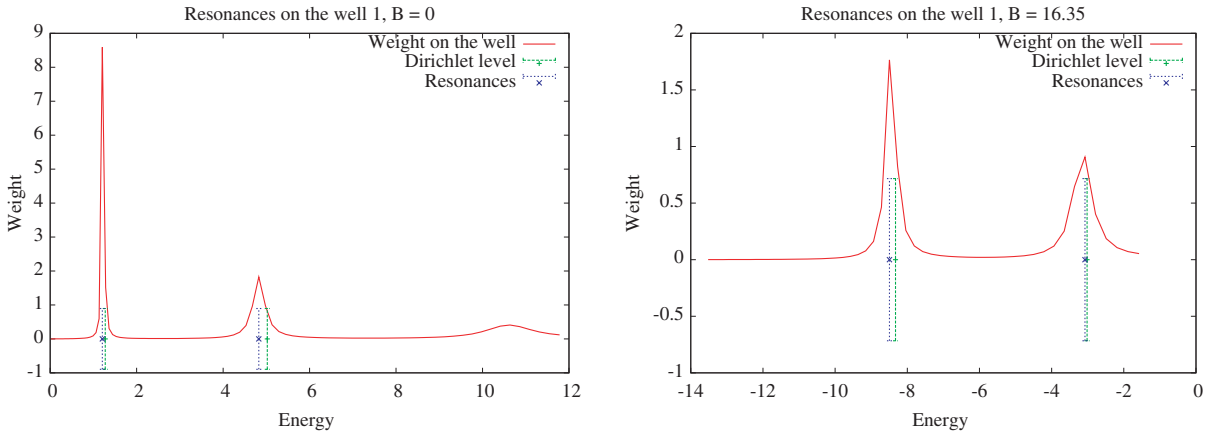

Fig. 3. Determination of resonant energies.

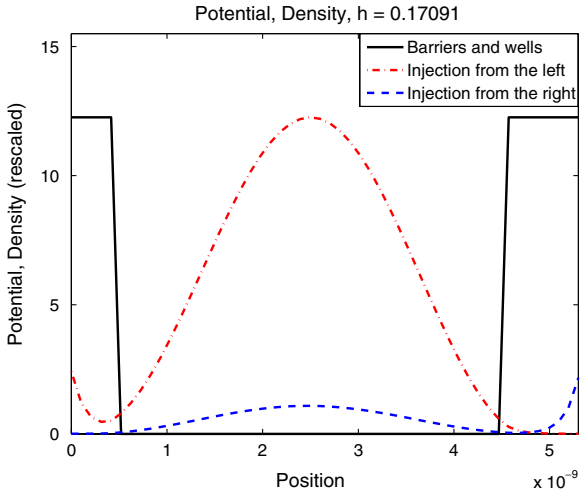

Fig. 4. Effect of injection from the left or from the right.

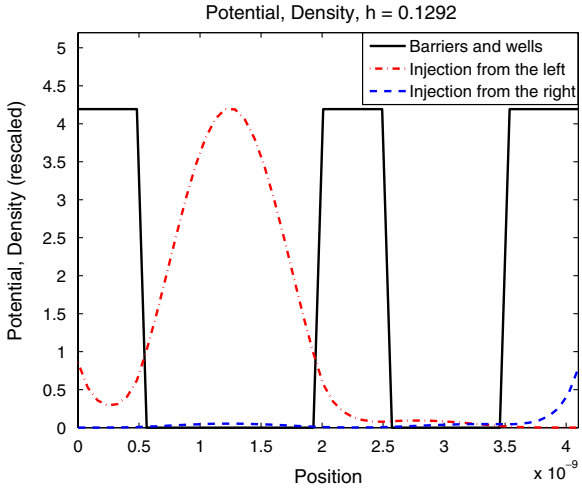

Fig. 5. Effect of injection from the left or from the right on a device with two wells.

$$d_{\mathrm{Ag}}(0, c_1; \mathscr{V} - E_1) < d_{\mathrm{Ag}}(c_1, 1; \mathscr{V} - E_1) \quad \text{and} \quad d_{\mathrm{Ag}}(0, c_2; \mathscr{V} - E_2) > d_{\mathrm{Ag}}(c_2, 1; \mathscr{V} - E_2).$$

If the electrons come only from the left, then (22) gives $t_1 = 1$ and $t_2 = 0$, in agreement with the numerical results. On the other hand, with injection from the right, no well is filled since the resonant energy E_2 in the second well is too high.

We will come back to this example in Section 9.2, case 4.

5.4. Piecewise affine potential

Restricting the nonlinear potential to the class of piecewise affine potential is the key point which permits to reduce the complexity of the full nonlinear system (11), in the limit $h \to 0$. It is a consequence of the scaling of the wells $W_j(\frac{x-c_j}{h})$ as quantum wells in a semiclassical island, for which the classically permitted region is asymptotically reduced to a single point. Nevertheless in practical cases, h is not 0 although reasonably small (according to the discussion of Section 5.2), and the wells have the same order of magnitude as the barriers. Hopefully, the nonlinearity is not very strong because the size of a well has the same order of magnitude of the Bohr radius a_{B}: the effective nonlinearity in the jth well is of order $\gamma_j = \frac{4L_j}{a_{\mathrm{B}}}$ after adapting the scaling (12) to a

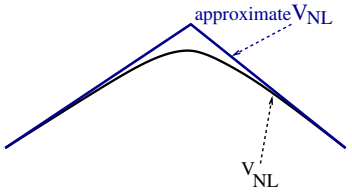

Fig. 6. Approximation of the nonlinear potential.

single well. Therefore, the difference between the true nonlinear potential and its piecewise affine approximation can be neglected when the position c_j is chosen close to the center of mass of the electronic density in the jth well according to Fig. 6.

The exactly used value of the position c_j is presented in Section 6.1.

6. Implementation of the asymptotic model

Here we show how the asymptotic model derived after taking the limit $h \to 0$ in Section 4 is adapted to physically relevant geometries for a finite value $h > 0$ of the parameter.

6.1. Position of the wells c_j and resonant depths e_j^k

Here we explain how the parameters c_j and e_j^k, $k = 1, \ldots, K_j$ are determined in realistic cases with $h > 0$. With those parameters, the kth resonant energy level attached to the jth well is given in the asymptotic model by

$$E_j^k = \tilde{\mathscr{V}}(c_j) - e_j^k, \tag{30}$$

according to (14) and (15). Actually, we restrict firstly our attention to the case $K_j = 1$ and write simply e_j instead of e_j^1. Fortunately, the process that we describe in this simpler case admits a natural and easily implementable extension to $K_j > 1$ by accepting several values c_j^k of the center of mass of the well. Details are given about this in the end of this paragraph and in Section 7.

The determination of c_j and e_j is done simultaneously without requiring additional heavy numerical computation. It is a linear interpolation process which relies on the following heuristic argument.

An intermediate step to show that the resonant energy in the jth well is close to $\tilde{\mathscr{V}}(c_j) - e_j$ relies on the fact that it is at a distance $\mathscr{O}(\mathrm{e}^{-c/h})$ from some eigenvalue of (28), with the energy-dependent absorbing boundary conditions replaced by homogeneous Dirichlet boundary conditions. Hence one can work with those Dirichlet eigenvalues, the eigenfunctions of which are localized in the quantum wells. Those Dirichlet eigenvalues admit a first order perturbation according to the Feynmann–Hellman law

$$\delta E = \langle \psi | \delta V \psi \rangle,$$

when ψ is a normalized eigenfunction at energy E, δV is the variation of the Hamiltonian and δE the corresponding variation of the eigenvalue. Moreover when $\delta V = \delta V(vx)$, with $v > 0$ small, varies on a slower scale than ψ, a second order Taylor expansion of $\delta V(c + v(x - c))$ leads to

$$\langle \psi | \delta V \psi \rangle = \int_0^1 \delta V(vx) |\psi(x)|^2 \, \mathrm{d}x = \delta V(c) + \mathscr{O}(v^2),$$

where c is the center of mass of the probability density $|\psi|^2$:

$$\int_0^1 (x - c) |\psi(x)|^2 \, \mathrm{d}x = 0.$$

The resonant energies associated with each well can be determined according to the process described in Section 5.2. These computations are done for the two extremal values of the applied bias, $B_{\min}$ and $B_{\max}$, and with no nonlinear potential ($V_{\mathrm{NL}}^h \equiv 0$). This provides in the well j the two resonant energies $E_j(B_{\min})$ and $E_j(B_{\max})$. The variation of the potential by changing the bias is the affine function $\delta V(x) = -(B_{\max} - B_{\min})x$ for $x \in [0, 1]$. The previous discussion says that the center of mass c_j can be approximated according to

$$E_j(B_{\max}) - E_j(B_{\min}) = -(B_{\max} - B_{\min})c_j. \tag{31}$$

Finally, the approximation $E_j \sim \tilde{V}(c_j) - e_j$ provides the value e_j by using

$$E_j(B) = V_0 - Bc_j - e_j, \tag{32}$$

applied with $B = B_{\max}$ or $B = B_{\min}$ (both are compatible according to (31)).

Fig. 7 summarizes how the parameters (c_j, e_j) (occurring in the asymptotic model $h \to 0$) are fitted to the numerical values of resonant energies ($h > 0$).

Fig. 8 shows in a practical case the actual density and the position c_j of the simplifying δ-function.

We end this paragraph with two remarks.

Remark 8

(1) The case of Fig. 8 seems at a first glance to be far from the situation of (narrow) quantum wells in a semiclassical island (wide barriers). Actually, the barriers can be considered as wide enough when they lead to a stiff localization of the resonant energies (see Section 5.2). On the other hand, replacing the real electronic density by a δ-function will not introduce a big error when the width of the well is less than the Bohr radius a_B.

(2) We focused on the case when there is one single resonant state per well. A simple way to introduce several resonant energies E_j^k per well, $1 \leqslant k \leqslant K_j$, can be done by determining several averaged positions according to (31), c_j^k, $1 \leqslant k \leqslant K_j$. This can also be interpreted as K_j wells separated by barriers with vanishing widths (see Fig. 10).

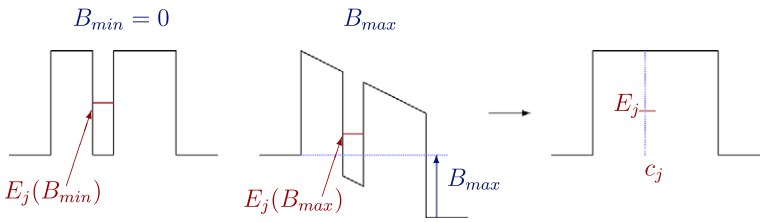

Fig. 7. Determination of the resonant depth e_j and of the averaged position c_j of the jth well.

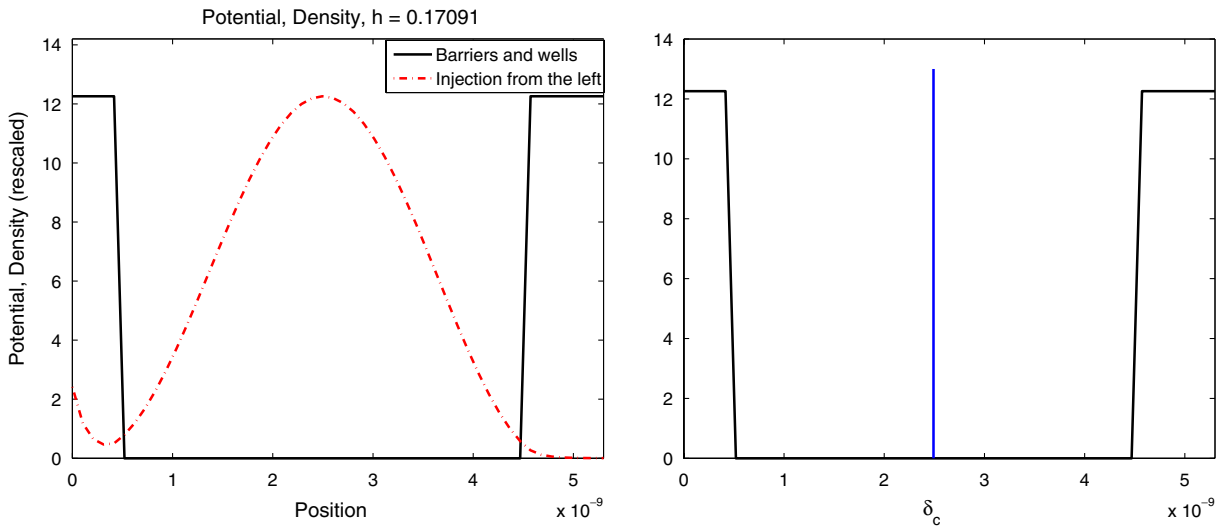

Fig. 8. Density on the well and position of the asymptotics well.

6.2. Current density

Another drawback of the asymptotic model obtained as $h \to 0$ is that the current density J defined in Section 3.5 vanishes as $h \to 0$. In the current–voltage characteristic curves which are presented here, the current density is computed for $h > 0$ with the help of the generalized eigenfunctions, once the nonlinear potential is computed with the asymptotic model. Hence the computation of the generalized eigenfunction which presents the highest complexity is done first to determine the parameters (c_j, e_j) of the asymptotic nonlinear problem and in the end in order to compute the current density.

7. Computation of Agmon distances for a piecewise affine potential

After Section 5.4, the nonlinear potential V_{NL}^h can be replaced by the piecewise affine asymptotic potential V of Theorem 5. Then the Agmon distances, which are involved in the definition of the different cases, admit an explicit algebraic expression which is specified here. Since small variations of the Agmon distances have a strong effect on the nonlinear problem, it is better here to compute these quantities with the real size of the wells and barriers. The left-hand side of Fig. 9 illustrates the asymptotics model with a total potential $\tilde{\mathscr{V}}$, which is piecewise affine, while the right-hand side presents a physically realistic case, with non-vanishing well widths, for which the potential is denoted $\mathscr{V} = \tilde{\mathscr{V}} + W$, with $-V_0 \leqslant W \leqslant 0$.

With the point c_i, the left and right ends of the barrier before c_i are denoted by c_i^- and c_i^+. For an energy $E \geqslant \max\{\mathscr{V}(x),\ x \in [c_i^+, c_{i+1}^-]\}$, the Agmon distances satisfy the relationship:

$$d_{\mathrm{Ag}}(c_i^-, c_i; \mathscr{V} - E) = d_{\mathrm{Ag}}(c_i^-, c_i^+; \tilde{\mathscr{V}} - E),$$

and

$$d_{\mathrm{Ag}}(c_i, c_{i+1}^+; \mathscr{V} - E) = d_{\mathrm{Ag}}(c_{i+1}^-, c_{i+1}^+; \tilde{\mathscr{V}} - E).$$

According to (30) and by considering only the case $K_i = 1$ according to Remark 8, the resonant energy attached to the well i equals:

$$E_i = \tilde{\mathscr{V}}(c_i) - e_i.$$

In agreement with all our numerical experiments, the non-negative resonant energies are assumed to lie above the bottom of the wells:

$$E_i \geqslant \max\left\{\mathscr{V}(x), x \in [c_k^+, c_{k+1}^-], 1 \leqslant k \leqslant N\right\} \quad \text{when } E_i \geqslant 0.$$

Then, the Agmon distances which are involved in the weight t_i, attached to the non-negative resonant energy $E_i \geqslant 0$, are given by

$$d_{-,i} = d_{\mathrm{Ag}}(0, c_i; \mathscr{V} - E_i) = \sum_{k=1}^{i} d_{\mathrm{Ag}}(c_{k-1}, c_k; \mathscr{V} - E_i) = \sum_{k=1}^{i} d_{\mathrm{Ag}}(c_k^-, c_k^+; \tilde{\mathscr{V}} - E_i), \tag{33}$$

and

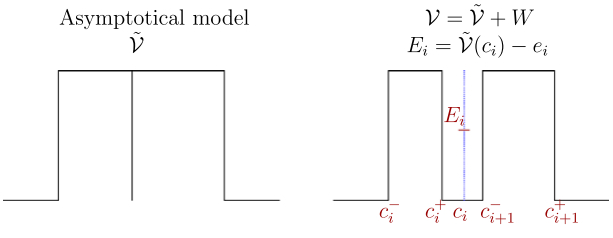

Fig. 9. Determination of the points characterizing a well.

$$d_{+,i} = d_{\mathrm{Ag}}(c_i, 1; \mathscr{V} - E_i) = \sum_{k=i+1}^{N+1} d_{\mathrm{Ag}}(c_{k-1}, c_k; \mathscr{V} - E_i) = \sum_{k=i+1}^{N+1} d_{\mathrm{Ag}}(c_k^-, c_k^+; \tilde{\mathscr{V}} - E_i), \tag{34}$$

with $c_0 = 0$ and $c_{N+1} = 1$. It remains to compute each term, $d_{\mathrm{Ag}}(c_k^-, c_k^+; \tilde{\mathscr{V}} - E_i)$. It is convenient to introduce the quantity

$$y_{k,i}^{\pm} = \frac{\tilde{\mathscr{V}}(c_k^{\pm}) - \tilde{\mathscr{V}}(c_i)}{e_i},$$

which permits to simplify the expression of $d_{\mathrm{Ag}}(c_k^-, c_k^+; \tilde{\mathscr{V}} - E_i)$ and to write

$$y_{k,i}^{\pm} \geqslant -1 \Longleftrightarrow E_i = \tilde{\mathscr{V}}(c_i) - e_i \leqslant \tilde{\mathscr{V}}(c_k^{\pm}).$$

Considering several cases illustrated by Fig. 10, the Agmon distance can be rewritten as

$$d_{i,-} = \frac{2}{3}\sqrt{e_i} \sum_{k=1}^{i} (c_k^+ - c_k^-)\mathsf{f}(y_k^+, y_k^-), \tag{35}$$

$$d_{+,i} = \frac{2}{3}\sqrt{e_i} \sum_{k=i+1}^{N+1} (c_k^+ - c_k^-)\mathsf{f}(y_k^+, y_k^-), \tag{36}$$

where the symmetric function f is given by

$$\mathsf{f}(y_1, y_2) = \begin{cases} \frac{(y_1+1)^{3/2} - (y_2+1)^{3/2}}{y_1 - y_2} & \text{if } y_1 \geqslant -1,\ y_2 \geqslant -1 \text{ and } y_1 \neq y_2, \\ \frac{3}{2}\sqrt{y_1 + 1} & \text{if } y_1 \geqslant -1,\ y_2 \geqslant -1 \text{ and } y_1 = y_2 + \mathrm{o}(1), \\ -\frac{(y_2+1)^{3/2}}{y_1 - y_2} & \text{if } y_1 \leqslant -1 \text{ and } y_2 \geqslant -1, \\ \frac{(y_1+1)^{3/2}}{y_1 - y_2} & \text{if } y_1 \geqslant -1 \text{ and } y_2 \leqslant -1, \\ 0 & \text{else.} \end{cases}$$

The Newton algorithm used in solving numerically the nonlinear problem also requires the expressions of the derivatives of (35) and (36). By setting $V_j = \tilde{\mathscr{V}}(c_j)$, the definition of $y_{k,i}^{\pm}$ leads to

$$\frac{\partial d_{i,-}}{\partial V_j} = \frac{2}{3}\sum_{k=1}^{i} \frac{(c_k - c_{k-1})(r_k^+ - r_k^-)}{\sqrt{e_i}} \times \Big[\big((1 - r_k^+)\partial_1\mathsf{f}(y_k^+, y_k^-) + (1 - r_k^-)\partial_1\mathsf{f}(y_k^-, y_k^+)\big)\delta_{k,j+1} + \big(r_k^+\partial_1\mathsf{f}(y_k^+, y_k^-) + r_k^-\partial_1\mathsf{f}(y_k^-, y_k^+)\big)\delta_{k,j} - \big(\partial_1\mathsf{f}(y_k^+, y_k^-) + \partial_1\mathsf{f}(y_k^-, y_k^+)\big)\delta_{i,j}\Big],$$

with $r_k^{\pm} = \frac{c_k^{\pm} - c_{k-1}}{c_k - c_{k-1}}$, for any $i,j \in \{1, \ldots, N\}$. The derivative $\partial_1\mathsf{f}$ equals

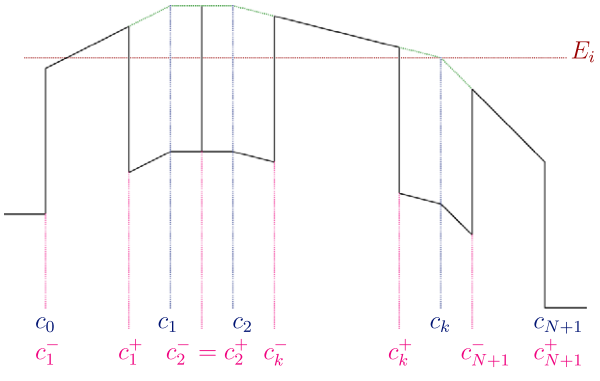

Fig. 10. Notation for a device.

$$\partial_1 f(y_1,y_2)=\begin{cases}\frac{\frac{3}{2}(y_1+1)^{1/2}(y_1-y_2)-(y_1+1)^{3/2}+(y_2+1)^{3/2}}{(y_1-y_2)^2} & \text{if } y_1\geqslant -1,\ y_2\geqslant -1 \text{ and } y_1\neq y_2,\\ \frac{3}{8}\frac{1}{\sqrt{y_1+1}} & \text{if } y_1\geqslant -1,\ y_2\geqslant -1 \text{ and } y_1=y_2+o(1),\\ \frac{(y_2+1)^{3/2}}{(y_1-y_2)^2} & \text{if } y_1\leqslant -1 \text{ and } y_2\geqslant -1,\\ \frac{\frac{3}{2}(y_1+1)^{1/2}(y_1-y_2)-(y_1+1)^{3/2}}{(y_1-y_2)^2} & \text{if } y_1\geqslant -1 \text{ and } y_2\leqslant -1,\\ 0 & \text{else.}\end{cases}$$

The derivative $\partial d_{+,i}/\partial V_j$ is obtained by summing over $k\in\{i+1,\dots,N+1\}$.

8. Penalization method

The constraints which involve the Agmon distance in Theorem 5 have no obvious convexity properties. The simplest and robust way to take them into account is a penalization method. Using notations (22), we set $t_j=\tau_j\theta_j$ with

$$\theta_j=\frac{1}{1+\exp\frac{d_{\mathrm{Ag}}(0,c_j;\tilde{\mathscr{V}}-E_j)-d_{\mathrm{Ag}}(c_j,1;\tilde{\mathscr{V}}-E_j)}{\varepsilon}},$$

and for any resonances, we distinguish three cases:

$$E_j=\tilde{\mathscr{V}}(c_j)-e_j>0,\quad \tau_j=1,$$
$$E_j=\tilde{\mathscr{V}}(c_j)-e_j<0,\quad \tau_j=0,$$
$$E_j=\tilde{\mathscr{V}}(c_j)-e_j=0,\quad \tau_j\in(0,1).$$

The penalization parameter $\varepsilon>0$ has to be small enough in order to have a realistic treatment of the constraint but not too small in order to keep a well-behaved Newton algorithm. In the original problem, the Agmon distances occur in factors which behave like $e^{\frac{d_{\mathrm{Ag}}(0,c_j;\tilde{\mathscr{V}}-E_j)-d_{\mathrm{Ag}}(c_j,1;\tilde{\mathscr{V}}-E_j)}{h}}$. Therefore, values between $\varepsilon=0$ and $\varepsilon=h$ make sense. The two extremal cases $\varepsilon=0$ and $\varepsilon=h$ have been tested. The possibility to take $\varepsilon=\mathscr{O}(h)$ implements a soft transition between $\theta_j=0$ and $\theta_j=1$ as it may occur when h is not very small.

The algorithm relies on a continuation for the 3^N cases corresponding to the three possible values of τ_j and the N wells. The critical case coming from the equality of the Agmon distance (only) in the case with two wells is treated separately.

The conditions $\tau_j\in[0,1]$, $E_j>0$, $E_j<0$ are verified a posteriori.

9. Numerical results

In this section, we show how our numerical approach is flexible and seems able to catch in a very efficient way the main quantities involved in the nonlinear problem. These computations were realized on a laptop with a Gnu Octave program (similar to MATLAB). The indicated "CPU time" refers to the CPU time in seconds used to solve the non linear problem without computing the current. The time used for this last part varies from one case to the other and can be significantly longer. The core of the program which is the rapid one permits to get very quickly an idea of the bifurcation diagram.

9.1. Computations for GaAs

We consider data of Pinaud proposed in [34,35]. Let us recall some physical parameters:

Relative mass	0.067
Relative permittivity	11.4
Temperature	300 K
Donor density	$10^{18}\,\mathrm{cm}^{-3}$

Fermi level E_F	0.054 eV
h	0.22
B_{min}	0 eV
B_{max}	0.25 eV
Height of barriers V_0	0.3 eV

We consider two devices with one well, the first with two barriers at equal size and the second with a barrier wider than the other. Data are given in Table 1 and illustrated in Fig. 11 for the case 1.

The results of the computations in case 1 and in case 2 are given in Figs. 12 and 13.

In case 1, we notice that there is no hysteresis phenomenon. The approximation of the current needs a fine discretization in energy. Those results are close to those of Pinaud [34]: For the same configuration, we obtain a similar magnitude for the current and the negative differential resistance occurs at the same position as in [34].

Table 1
Data of the GaAs devices

	Case 1	Case 2
Size of the first barrier (nm)	5	3
Size of the second barrier (nm)	5	6
Size of the well (nm)	5	6
Penalization parameter ε	0.001	0.01
♯ of voltage values B	100	100
♯ of momentum values k	1000	200
Position of the well (nm)	$c_1 = 7.8$	$c_1 = 6.3$
Resonance depth e_1 (eV)	0.21	0.227
CPU time (s)	9.21	9.22

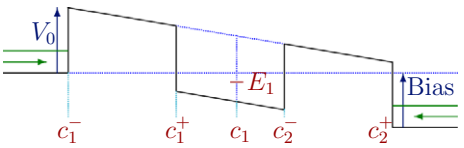

Fig. 11. Device of the case 1.

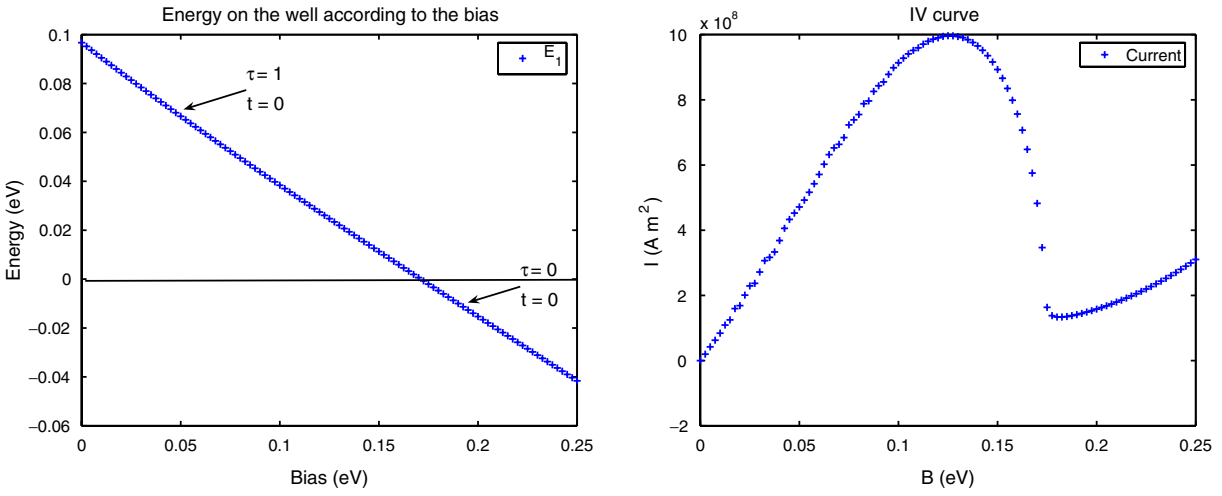

Fig. 12. Case 1. Negative differential resistance.

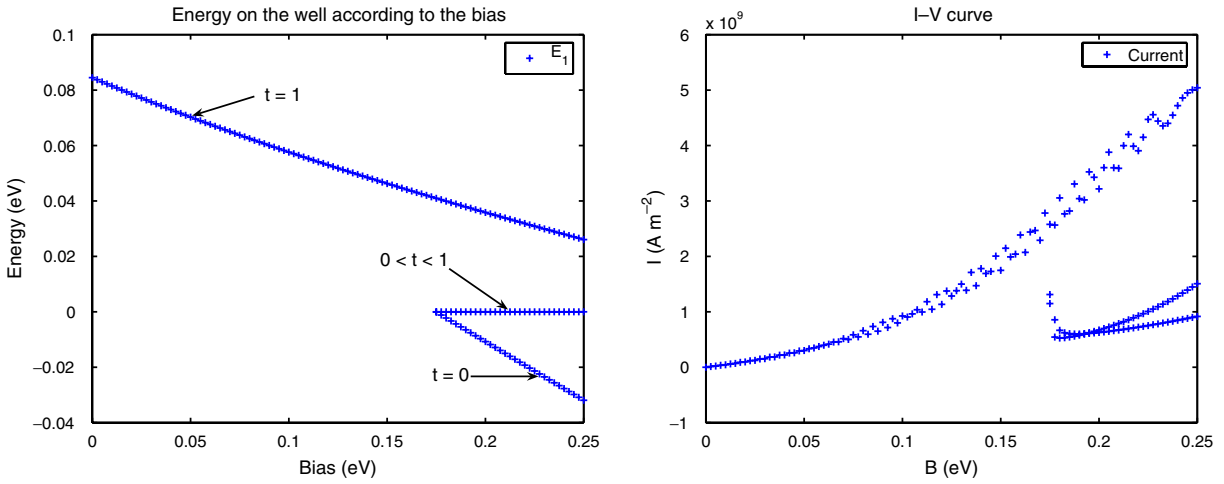

Fig. 13. Case 2. Hysteresis phenomenum.

In case 2, we observe a hysteresis phenomenon. The hysteresis curve is not complete here. Actually, after trying several configurations, obtaining a complete hysteresis phenomenon appeared rather difficult in GaAs–AlGaAs heterostructures (the barriers are not high enough).

9.2. Computations for Si

We now consider five devices in Si–SiO whose common physical parameters are

Relative mass	$(0.19, 0.92, 0.19)$
Relative permitivity	11.9
Temperature	300 K

Table 2 gives the geometry, physical and numerical parameters of the test cases.

The characteristics data of case 1 are taken from [26]. In this example where the two barriers have the same size, several values of the penalization parameter were tested according to the discussion of Section 8 and led here to interesting variations. Fig. 14 was obtained with a smaller parameter $\varepsilon = 0.01$ while Fig. 15 shows the results for $\varepsilon = h \sim 0.3$. If the penalization parameter is small, $\varepsilon = 0.01$, then no hysteresis phenomenon appears as shown in Fig. 14 (CPU time is equal to 38.2). The resonant energies vary linearly and only the negative differential resistance remains on the I–V curve of Fig. 14.

The second choice of the penalization parameter, $\varepsilon = h = 0.301933$, shows in Fig. 15 a small double hysteresis phenomenon for biases in agreement with the ones obtained in [26] (the CPU time was 54.57).

Actually, the sensitivity to the penalization parameter is due to the fact that this case, with two equal barriers, shows rather small differences between the right and left Agmon distances. Practically this would mean that the hysteresis phenomenon (or its absence) is rather unstable with respect to small variations of the data. As this is shown below, and confirmed by other numerical experiments in [31], the hysteresis phenomenon can be strengthened when the second barrier is wider than the first one. On the contrary, it disappears as the width of the second barrier becomes significantly smaller than the first one. The choice of a penalization parameter close to $h > 0$ broadens this transition.

Looking at case 2 (see Fig. 16), the hysteresis appears more easily with the silicon heterostructures than with the GaAs ones and it is more intensive, as it appears in Fig. 16. In comparison with the first silicon device (case 1), the width of the second barrier and of the well have been increased. This makes the hysteresis phenomena more stable and it is not sensitive to the variations of the penalization parameter like in of Section 9.1, case 2.

Table 2
Data for the silicon devices

	Case 1	Case 2	Case 3	Case 4	Case 5
Donor density, n_D (cm^{-3})	10^{20}	10^{20}	10^{20}	5×10^{20}	5×10^{20}
Fermi level, E_F (eV)	0.245	0.245	0.245	0.716	0.716
B_{min} (eV)	0	0	0	0	0
B_{max} (eV)	4	3	2.5	2.5	3
Height of barrier, V_0 (eV)	3	3	3	3	3
Number of wells	1	1	2	2	4
Size of the first barrier (nm)	0.5	0.5	0.5	0.5	0.5
Size of the second barrier (nm)	0.5	1	0.5	0.5	0.5
Size of the third barrier (nm)			1	0.6	0.5
Size of the fourth barrier (nm)					0.5
Size of the first well (nm)	2	2.5	1.5	1.5	1
Size of the second well (nm)			1	1	1
Size of the third well (nm)					0.5
Size of the fourth well (nm)					0.5
h	0.301933	0.22	0.2	0.13	0.13
Penalization parameter ε	0.01/0.301933	0.01	0.01	0.01	0.096
♯ of voltage values B	100	100	100	100	100
♯ of momentum values k	200	200	200	200	400
Number of resonant energies	2	2	2	2	4
Position of the well c_1 (nm)	1.46	1.7	1.2	1.2	1.1
Position of the well c_2 (nm)	1.77	2.1	3	3	2.4
Position of the well c_3 (nm)					3.9
Position of the well c_4 (nm)					4.5
Position of the well c_5 (nm)					5.5
Resonance depth e_1 (eV)	1.8	2.2	2.5	2.5	2.09
Resonance depth e_2 (eV)	2.7	2.8	2.7	2.1	2.24
Resonance depth e_3 (eV)					1.1
Resonance depth e_4 (eV)					1.68
CPU time (s)	38.2/54.57	45.5	42.45	84.99	528.63

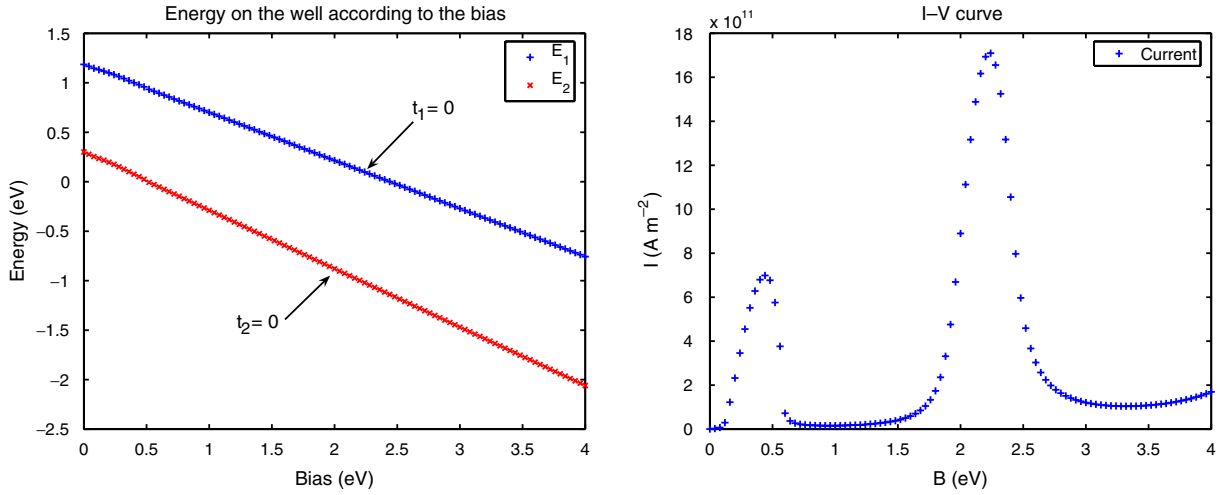

Fig. 14. Case 1. Small penalization parameter.

In case 3 (see Fig. 17), the very high barrier potentials permit to create cases with a double well were the two (asymptotic) resonant energies eventually take the same value. The second resonant energy decreases faster than the first one. They reach the same value for the bias $B \sim 1$ eV and a new bifurcation branch

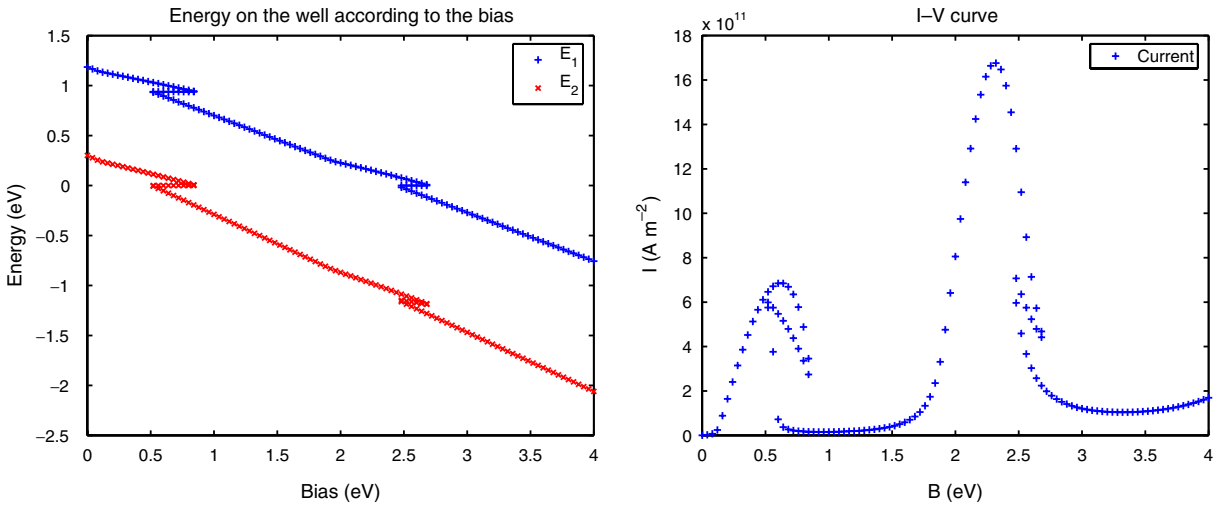

Fig. 15. Case 1. Penalization parameter of size h.

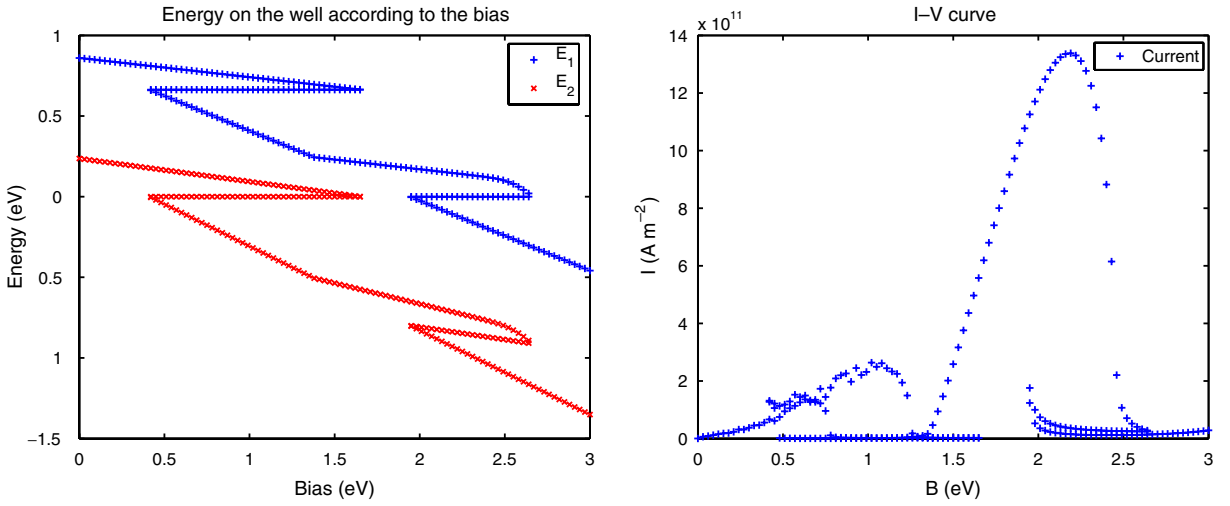

Fig. 16. Case 2. Hysteresis.

seems to develop. This last point is even more obvious in the next case. Note that there is a small piece of hysteresis phenomenon for a high applied voltage. It is coupled with an apparently strange behaviour of the current density, for $1.7\ \text{eV} \leqslant B \leqslant 2\ \text{eV}$. Actually, it is an artefact of our approach: the nonlinear potential is essentially determined via the asymptotic model while the current is computed with the full linear Schrödinger system once the potential is known. The bias for which the resonant energy crosses the value 0 is not exactly detected with the asymptotic model. This generates a substancial error on the current density at this moment.

In case 4 (see Fig. 18), we now consider a case similar to case 3, with a donor density equal to $5 \times 10^{20}\ \text{cm}^{-3}$. With two wells and according to the discussion of [31–33] summarized in Section 4.1, some critical cases are possible depending on the comparison of the two extremal Agmon distances. This is produced in the next example in which the first and third barriers have almost the same size.

The last example (case 5) is a device with four wells. The bifurcation diagram, presented in Fig. 19, in which only the generic cases were considered (no specific solution due to the crossing of resonant energies) demonstrates a complex interaction between the different resonant levels.

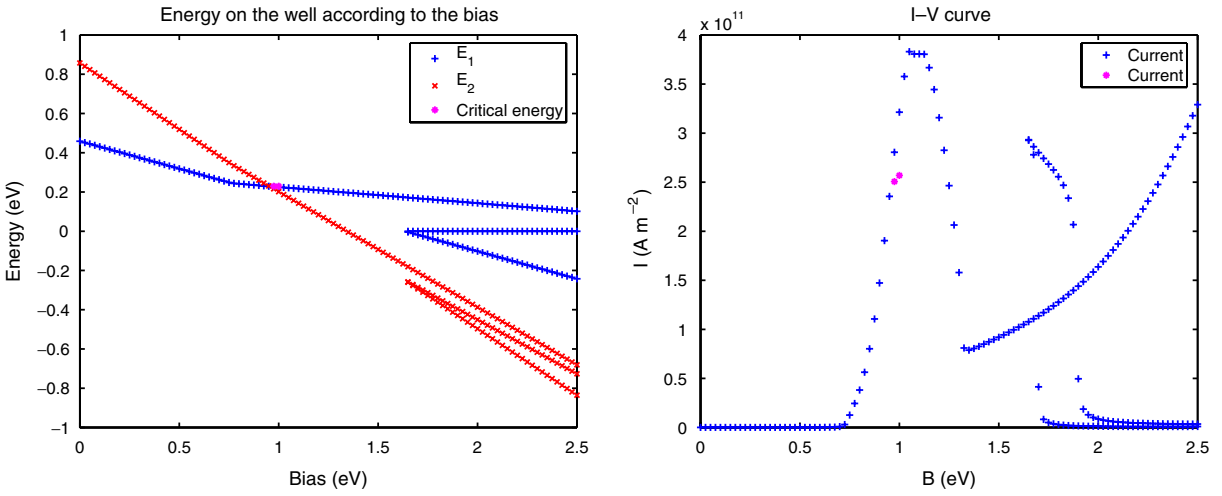

Fig. 17. Case 3. Crossing and Hysteresis.

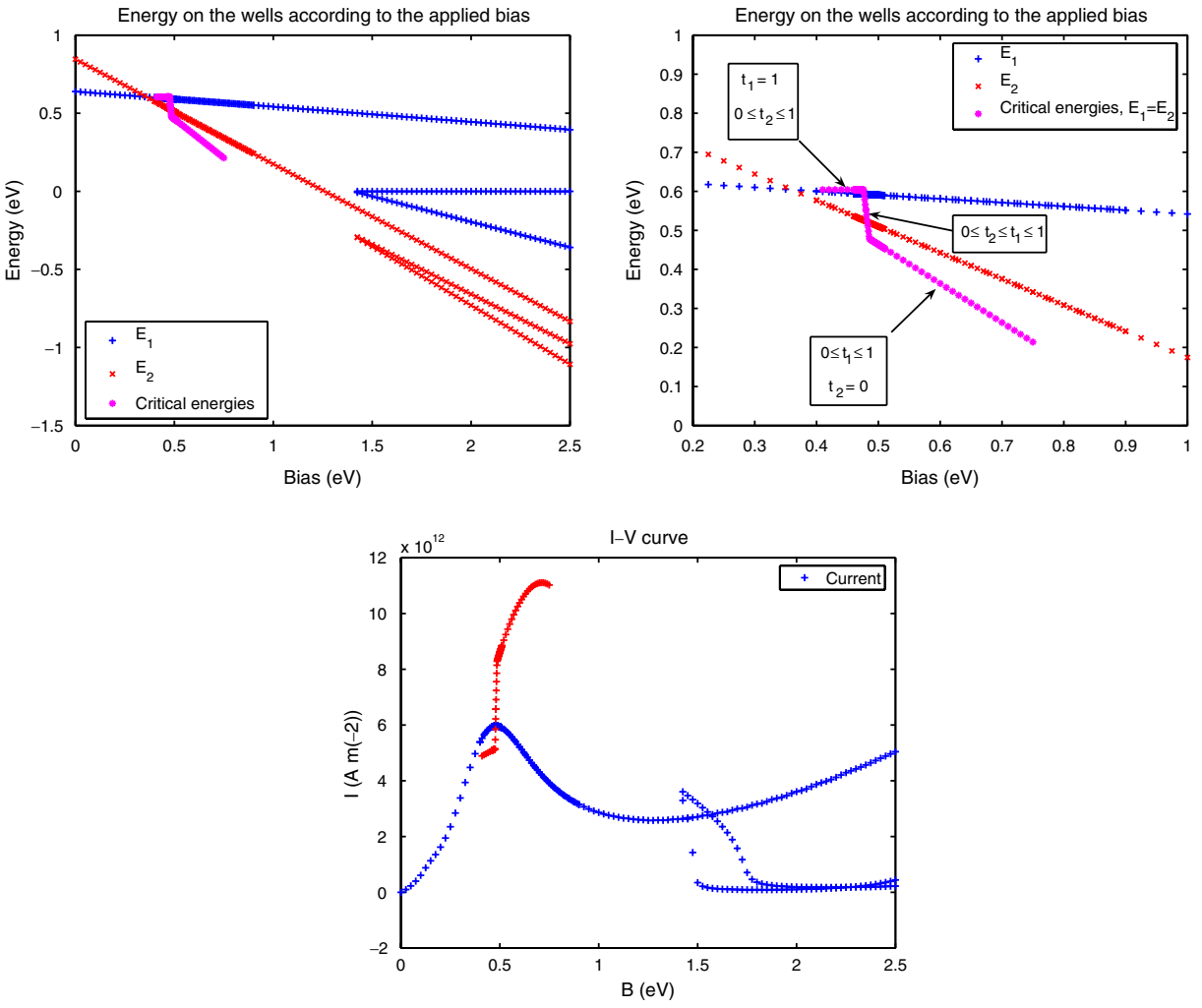

Fig. 18. Case 4. Critical solutions.

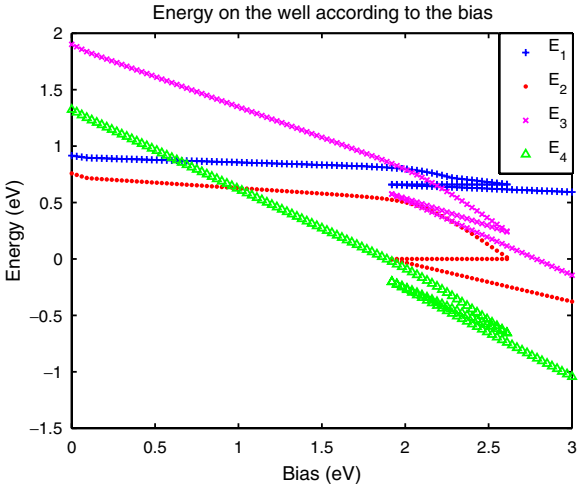

Fig. 19. Case 5. Solutions for a device with four wells.

10. Conclusion

The numerical experiments of Section 9 have shown on realistic cases that rather complex bifurcation diagrams can occur and are numerically accessible. This extends the previous works which were concerned with the hysteresis phenomenon (see for example [21,37]). Our model permits to get very rapidly the shape of the bifurcation diagram. It relies on rigorous mathematical results concerned with the asymptotic regime of quantum wells in a semiclassical island, given in [32,33]. Although the asymptotic model required some modifications in order to fit with the parameters of realistic devices, the numerical results turn out to be close to the ones of [26,34,35] based on a full treatment of the Schrödinger–Poisson system in the Landauer–Büttiker approach.

Those calculations must not be considered as final ones. Firstly, as it is discussed after Fig. 17, the values of the current density have to be interpreted with some care. Secondly, our model does not take into account the nonlinear effect outside the quantum wells-barriers structure. Actually, the space-charge effects in those area have been shown to be significant in some cases according to [27]. Finally, the asymptotic model on which those calculations are based detects all the possible asymptotic solutions, without discriminating whether these solutions really exist or not. For example and even without considering the stability question, it is not clear that the detected critical solution of Fig. 18 really exists or is replaced by some nonlinear beating effect like in [16,17].

Nevertheless these drawbacks are compensated by the rapidity of the method. This numerical approach can first be used in order to get an insight of the influence of the data (geometry and height of the barriers, donor density, temperature, applied bias, etc.) on the shape of the bifurcation diagram. Finally, when several nonlinear solutions are possible, a Newton algorithm for complete simulations of the Schrödinger–Poisson system requires an initial guess. This approach provides it.

Acknowledgements

The authors thank N. Ben Abdallah, F. Mehats, C. Presilla, J. Sjöstrand, O. Vanbésien and B. Vinter for remarks and discussions about this work. They were partly supported by the french ACI no. 1034 "Systèmes hors-équilibre quantiques et classiques".

References

[1] A. Arnold, Numerical absorbing boundary conditions for quantum evolution equation, VLSI Des. 6 (1–4) (1998) 313–319.

[2] A. Arnold, Mathematical concepts of open quantum boundary conditions, Transp. Theory Stat. Phys. 30 (4–6) (2001) 561–584.
[3] M. Baro, N. Ben Abdallah, P. Degond, A 1D coupled Schrödinger drift-diffusion model including collisions, J. Comput. Phys. 203 (2005) 129–153.
[4] M. Baro, H. Neidhardt, J. Rehberg, Current coupling of drift-diffusion models and Schrödinger–Poisson systems: dissipative hybrid models, SIAM J. Math. Anal. 37 (3) (2005) 941–981.
[5] N. Ben Abdallah, On a multidimensional Schrödinger–Poisson scattering model for semiconductors, J. Math. Phys. 41 (7) (2000) 4241–4261.
[6] N. Ben Abdallah, P. Degond, P.A. Markowich, On a one-dimensional Schrödinger–Poisson scattering model, Z. Angew. Math. Phys. 48 (1) (1997) 135–155.
[7] N. Ben Abdallah, O. Pinaud, Multiscale simulation of transport in an open quantum system: resonances and WKB interpolation, J. Comput. Phys. 213 (1) (2006) 288–310.
[8] M. Büttiker, Y. Inry, R. Landauer, S. Pinhas, Generalized many-channel conductance formula with application to small rings, Phys. Rev. B 31 (1985) 6207–6215.
[9] P. Caussignac, J. Descloux, A. Yamnahakki, Simulation of some quantum models for semiconductors, Math. Models Methods Appl. Sci. 12 (8) (2002) 1049–1074.
[10] Z. Chen, A finite element method for the quantum hydrodynamic model for semiconductor devices, Comput. Math. Appl. 31 (7) (1996) 17–26.
[11] Z. Chen, B. Cockburn, C.L. Gardner, J.W. Jerome, Quantum hydrodynamic simulation of hysteresis in the resonant tunneling diode, J. Comput. Phys. 117 (2) (1995) 274–280.
[12] F. Chevoir, B. Vinter, Scattering assisted tunneling in double barriers diode: scattering rates and valley current, Phys. Rev. B 47 (1993) 7260–7274.
[13] P. Degond, F. Mehats, C. Ringhofer, Quantum energy transport and drift diffusion models, J. Stat. Phys. 118 (3–4) (2005) 625–665.
[14] W.R. Frensley, Boundary conditions for open quantum systems driven for equilibrium, Rev. Mod. Phys. 62 (3) (1990) 745–791.
[15] C. Gérard, A. Martinez, Semiclassical asymptotics for the spectral function of long-range Schrödinger operators, J. Funct. Anal. 84 (1) (1989) 226–254.
[16] V. Grecchi, A. Martinez, A. Sacchetti, Double well Stark effect: crossing and anticrossing of resonances, Asymptotic Anal. 13 (4) (1996) 373–391.
[17] V. Grecchi, A. Martinez, A. Sacchetti, Destruction of the beating effect for a non-linear Schrödinger equation, Commun. Math. Phys. 227 (1) (2002) 191–209.
[18] B. Helffer, Semi-classical Analysis for the Schrödinger Operator and Applications, Lecture Notes in Mathematics, vol. 1336, Springer, Berlin, 1988.
[19] B. Helffer, J. Sjöstrand, Résonances en limite semi-classique, Mém. Soc. Math. France (N.S.) 24–25 (1986) iv+228.
[20] P.D. Hislop, I.M. Sigal, Introduction to Spectral Theory, Applied Mathematical Sciences, vol. 113, Springer, New York, 1996.
[21] G. Jona-Lasinio, C. Presilla, J. Sjöstrand, On Schrödinger equations with concentrated nonlinearities, Ann. Phys. 240 (1) (1995) 1–21.
[22] J. Kastrup, R. Klann, H. Grahn, K. Ploog, L. Bonilla, J. Galán, M. Kindelan, M. Moscoso, R. Merlin, Self-oscillations of domains in doped GaAs–AlAs superlattices, Phys. Rev. B 52 (1995) 13761–13764.
[24] A.M. Kriman, N.C. Kluksdahl, D.K. Ferry, Scattering states and distribution functions for microstructures, Phys. Rev. B 36 (1987) 5953–5959.
[25] R. Landauer, Spatial variation of currents and fields due to localized scatterers in metallic conduction, IBM J. Res. Dev. 1 (1957) 223–231.
[26] S.E. Laux, A. Kumar, M.V. Fischetti, Analysis of quantum ballistic electron transport in ultra-small semiconductor devices including space-charge effects, J. Appl. Phys. 95 (2004) 5545–5582.
[27] P. Mounaix, O. Vanbésien, D. Lippens, Effects of cathode space layer on the current–voltage characteristics of resonant tunneling diodes, Appl. Phys. Lett. 57 (8) (1990) 1517–1519.
[30] F. Nier, The dynamics of some quantum open systems with short-range nonlinearities, Nonlinearity 11 (4) (1998) 1127–1172.
[31] F. Nier, Y. Patel, Nonlinear asymptotics for quantum out of equilibrium 1D systems: reduced models and algorithms, in: Conference "Multiscale Methods in Quantum Mechanics and Experiments", Accademia dei Lincei Roma.
[32] Y. Patel, Développements de modèles macroscopiques pour des systèmes quantiques non-linéaires hors-équilibre, Thèse de doctorat, Université de Rennes I, 2005.
[33] Y. Patel, Steady states of 1D-Schrödinger–Poisson systems with quantum wells I (in preparation).
[34] O. Pinaud, Transient simulations of a resonant tunneling diode, J. Appl. Phys. 92 (4) (2002) 1987–1994.
[35] O. Pinaud, Analyse mathématique et numérique de quelques problèmes de transport dans les nanostructures, Thèse de doctorat, Université Paul Sabatier de Toulouse, 2003.
[36] R. Pinnau, A. Unterreitter, The stationary current–voltage characteristics of the quantum drift-diffusion model, SIAM J. Numer. Anal. 37 (1) (1999) 211–245.
[37] C. Presilla, J. Sjöstrand, Transport properties in resonant tunneling heterostructures, J. Math. Phys. 37 (10) (1996) 4816–4844.
[38] M. Reed, B. Simon, Methods of Modern Mathematical Physics. IV. Analysis of Operators, Academic Press [Harcourt Brace Jovanovich Publishers], New York, 1978.